Seasonal methane emissions from Lagoon Pingo West in Svalbard

THESIS FOR THE DEGREE OF

BACHELOR OF SCIENCE (B.Sc.)

at the

Institute of Environmental Science and Geography

of the

University of Potsdam

Helene Köhnen
Matriculation Number: 796605

POTSDAM
AUGUST 22, 2022

Supervisors:
Dr. Claire Treat, Prof. Ulrike Herzschuh, Prof. Andrew J. Hodson

Contents

List of Figures

List of Tables

Zusammenfassung

Methan ist ein Treibhausgas, welches die Wirkung von Kohlendioxid bei weitem übertrifft. Daher ist es wichtig, Methanemissionen zu messen. Aktuelle Studien zu natürlichen Methanemissionen in der Arktis befassen sich mit der Methanfreisetzung im Auftaubereich des Permafrosts und der obersten Schicht der darunterliegenden Sedimente und Gesteine, beispielsweise in Feuchtgebieten. Pingos, die im Permafrost entstandene Erdhügel mit einem inneren Eiskern sind, können im Gegensatz dazu Methan aus Anreicherungen im Grundwasser unter dem Permafrost freisetzen. Während der Sommersaison können die eishaltigen Bereiche eines Pingos auftauen und einen See bilden. Während einer Studie in Svalbard im Sommer 2017, wurden Proben aus einem See eines Pingos entnommen und die enthaltene Methankonzentration gemessen. Auf dieser Basis wurde der Methanfluss in die Atmosphäre modelliert. Der saisonale Methanfluss war mit 46.0 $gCH_4 \cdot 100\ d \cdot m^{-2}$ höher als der der umliegenden Feuchtgebiete. Daher werden Pingos "Emissions-Hotspots" in der arktischen Landschaft Spitzbergens genannt. Diese Studie zielt darauf ab, die Methankonzentration und den Methanfluss von einem See eines Pingos für die Sommersaison 2020 und 2021 zu quantifizieren. Dieser See heißt Lagoon Pingo West und erhält Wasser aus derselben Quelle, wie der nahe gelegene See Lagoon Pingo East, wo die Studie 2017 durchgeführt wurde. Ich habe an 11 Tagen im Sommer Proben des Seewassers genommen, wobei die Zeitabstände zwichen den Proben zwischen 3 und 16 Tagen varierten. Die Proben wurden im Labor hinsichtlich ihres Methangehalts untersucht. Zusätzlich habe ich einen automatischen Methananalysator verwendet, der die Methankonzentration stündlich gemessen hat. Der Methanfluss wurde mithilfe eines Diffusionsmodells berechnet, für das die Ergebnisse der Proben und des Analysators verwendet wurden. Im August 2021 konnte ich Kammermessungen durchführen, die Schätzungen über den Methanfluss ermöglichten. Ich fand in der Nähe des Zuflusses im zentralen Teil des Sees höhere Methankonzentrationen als an den Rändern oder am Abfluss. Ich konnte ein saisonales Muster in der Methankonzentration beobachten, das für die Positionen und Jahre unterschiedlich war. Alle Daten zeigten jedoch niedrige Methankonzentrationen nach der Schmelzsaison. Der saisonale Mittelwert des Methanflusses war 2021 höher als 2020. Das Diffusionsmodell auf Basis des Analysators lieferte höhere Ergebnisse als die Kammermessungen. Die Ergebnisse unter Verwendung des Diffusionsmodells, die auf den Proben basierten, waren am niedrigsten. Die Studie zeigte, dass der Methanfluss in beiden Jahren niedriger war als der Methanfluss von Lagoon Pingo East in 2017. Der saisonale Methanfluss betrug in 2020 etwa 1.69 $gCH_4 \cdot 100\ d \cdot m^{-2}$, welches ein Durchschnittswert der Positionen im See ist, und in 2021 8.17 $gCH_4 \cdot 100\ d \cdot m^{-2}$. Die Ergebnisse sind jedoch immer noch höher als mittlere Schätzungen von anderen arktischen Seen. Zukünftige Arbeiten könnten die Zeitabstände, in denen Proben des Seewassers entnommen werden, verringern, um den saisonalen Verlauf der Methankonzentration besser zu verstehen. Sie könnten außerdem täglich oder wöchentlich die Freisetzung von methanhaltigen Blasen des Seewassers erfassen, welche zu den Methanemissionen beiträgt.

Abstract

Methane is a potent greenhouse gas, with an even stronger climate forcing than carbon dioxide. Therefore, it is important to measure methane emissions. Recent studies on natural methane emissions from the Arctic, focused on methane release from the active layer and shallow permafrost, for example in wetlands. In contrast, pingos might act as emission sources for methane from reservoirs beneath the permafrost. A pingo is a landform in permafrost with an inner ice-core. Over the summer season, the icy parts of the pingo might thaw and form a lake. A study in Svalbard in the summer of 2017, measured the methane concentration in samples of a pingo lake, and modelled the flux of methane to the atmosphere. The seasonal methane flux amounted to 46.0 $gCH_4 \cdot 100\ d \cdot m^{-2}$. As the seasonal flux was higher than those of surrounding wetlands, pingos were characterized as "emission hotspots" in the Arctic landscape of Svalbard. This study aims to quantify the methane concentration and methane flux from Lagoon Pingo West for the summer seasons of 2020 and 2021. Lagoon Pingo West is fed by the same pingo spring as Lagoon Pingo East, where the study has been conducted in 2017. I used 11 samples over the summer season taken in irregular time intervals between 3–16 days to monitor the methane concentration. In addition, I used an automatic methane analyzer that measured the methane concentration in one-hour steps. The methane flux was calculated using a diffusion model that employed the results of the samples and the analyzer. In August 2021, I could apply chamber measurements that allowed for estimates of the methane flux. I found higher methane concentrations near the inflow in the central part of the lake than at the margins or at the outflow. I could observe a seasonal pattern in methane concentration, that varied with the positions and years. However, all data showed low methane concentrations after the melt season. The seasonal mean of the methane flux was higher in 2021 than in 2020. The diffusion model, using the analyzer data yielded higher results than the chamber measurements. The lowest results were obtained using the diffusion model with the data of the samples. The estimates for the seasonal methane fluxes were lower than those of Lagoon Pingo East in 2017. In 2020, the seasonal flux amounted to 1.69 $gCH_4 \cdot 100\ d \cdot m^{-2}$ at Lagoon Pingo West, calculated for the average of the sample positions, and in 2021 it amounted to 8.17 $gCH_4 \cdot 100\ d \cdot m^{-2}$. The results show that the methane flux from Lagoon Pingo West is higher than estimates from other Arctic lakes. In future works, the frequency of sampling could be increased to better understand the seasonal pattern of the methane concentration. The estimates of methane fluxes could be improved by daily or weekly measurements of the ebullition flux from the lake water.

Keywords: Methane, Climate, Diffusion model, Chamber measurements, High Arctic, Open-system pingo, Svalbard

Abbreviations: CH_4 - Methane; CO_2 - Carbon dioxide; DOY - Day of the year; EC - Electrical conductivity; LP - Lagoon Pingo; LP East - Lagoon Pingo East; LP West - Lagoon Pingo West; ORP - Oxidation-reduction-potential; PSU - Practical Salinity Unit; WMS - Web Map Service

1 Introduction

1.1 Motivation

Methane (CH_4) is an important greenhouse gas in the Earth's atmosphere, characterized by a greenhouse forcing 25 times greater than carbon dioxide (CO_2) on time scales of 100 years (Forster et al., 2007). The total methane emissions to the atmosphere are estimated to range between 500 and 600 $TgCH_4 \cdot y^{-1}$ (Lecher et al., 2017). However, there are uncertainties to this budget, which can largely be attributed to natural emissions from permafrost and the sub-permafrost environment (Kraev et al., 2019), including pingos (Hodson et al., 2019). Pingos are landforms in permafrost, which can release methane through aquatic diffusion during the summer season. The summer fluxes of Lagoon Pingo East (LP East) in Svalbard have been shown to exceed fluxes measured in wetlands in the surrounding landscapes (Hodson et al., 2019). Therefore, pingos were characterized as "emissions hotspots" (Hodson et al., 2019). The aim of this study is to quantify the concentration of dissolved methane in Lagoon Pingo West (LP West), and the methane emissions during the summer seasons of 2020 and 2021, to contribute to a better understanding of pingos and their potential impact on the climate. As the ecological, economic and social consequences of climate change become more explicit (Carleton and Hsiang, 2016), it is crucial to resolve the uncertainty in estimates of methane emissions, including those from remote regions in the Arctic.

1.2 Geomorphology of Pingos

To understand pingos, it is important to recall the concept of permafrost. Permafrost is defined as ground that has a temperature of 0 °C or colder for two or more consecutive years. In the permafrost regions, the upper layer of soil and sediments typically thaws during the summer season. This is called the active layer (Heginbottom et al., 2012). Permafrost below the active layer retards the vertical movement and exchange of water. However, perennially unfrozen zones, for example at the base of glaciers or under lakes, may allow for groundwater percolation. Pingos might emerge where groundwater is able to move to the surface (Hornum, 2018).
Pingos consist of a core of massive ice, produced primarily by the injection of water in permafrost. The expansion of the ice-core leads to the up-doming of surface strata.
The emerging hill can reach a height of up to 70 m (Mackay, 1998). At some pingos, water collects in small ponds or lakes during the summer season.
Pingos can be divided into two types. The first is known as the closed-system (Porsild, 1938; Müller, 1959), or hydrostatic pingo (Mackay, 1979). There are numerous examples of this type, for example in the Mackenzie Delta in Canada. The formation of this type of pingo is associated with the drainage of a lake. Downwards freezing of the sediments results in the expulsion of pore water. Above the previously saturated sediments, the expelled water collects and refreezes, isolated from the surface through the active layer (Porsild, 1938; Mackay, 1998).
The other class is the open-system pingo or hydraulic pingo. There are many examples in the ice-free regions of Greenland, in the mountain regions of northern Russia, and in Svalbard (Heginbottom et al., 2012). Open-system pingos develop when intrapermafrost or sub-permafrost groundwater reaches the surface due to artesian pressure (French, 2007; Worsley and Gurney, 1996). There are three groups of open-system pingos, based on their position in the landscape (Yoshikawa and Harada, 1995): (a) those above geological faults; (b) those at the foot of polythermal glaciers; (c) those occurring in recently emerged coastal lowlands.
Pingos of group (a) are fed by groundwater which migrates through geological faults to the surface. However, it is not known how the artesian pressure is generated for this group of pingos (Hornum, 2018). Pingos of group (b) form at the foot of glaciers, where meltwater from the base of the glacier is able to percolate into aquifers below the permafrost.

As a consequence, the pressure in the groundwater body increases and induces the formation of pingo springs at a low point in the topography (Liestøl, 1977).
Recent research focused on the formation of open-system pingos of group (c) (Hornum et al., 2020). The formation is induced through a negative shift in the surface energy balance, typically after isostatic rebound. Isostatic rebound is the rise of land masses that were depressed by the huge weight of ice sheets during the last ice age (NSIDC, 2022). As permafrost aggrades, water freezes in the pore space and hence expands. From a certain depth downwards, the lithostatic pressure inhibits ground heave, and the ice expansion induces an overpressure on the sub-permafrost groundwater. As a consequence, groundwater might flow to the surface and form a pingo, as depicted in Figure 1. The formation of a pingo of group (c) resembles the closed-system type. However, the time-scales of the formation are much longer and the sediments from where the pore water is expelled are not enclosed in permafrost (Hornum et al., 2020).

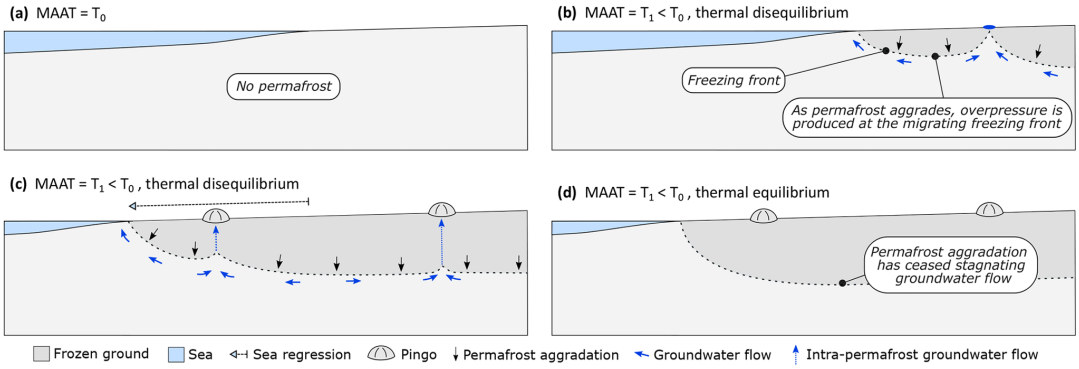

Figure 1: Pingo formation in near shore areas, by Hornum et al. (2020): (a) No permafrost is present. Mean Annual Air Temperature (MAAT) = T_0; (b, c) Permafrost expansion due to a decrease of the MAAT. Pressure is induced at the freezing front, groundwater is forced to the surface where a pingo forms; (d) Permafrost expansion has stagnated, the pingo might become inactive.

1.3 Methane in Pingos

Methane, in pingos with active springs, might originate from the sub-permafrost environment and be transported to the surface with the upwelling water (Hodson et al., 2019).
The two dominant processes that generate methane beneath the permafrost are: methane production by methanogenic microorganisms, known as "biogenic" methane; and methane production during the breakdown of larger organic molecules under elevated temperatures and pressure, termed "thermogenic" methane (Walter Anthony et al., 2012; Stolper et al., 2015).
Both biogenic and thermogenic methane, of different ages, could be trapped in form of clathrates in zones of cold temperatures and high pressure, several hundred meters deep beneath pingos (Betlem et al., 2018). Clathrates are ice-like crystalline solids composed of water and gas (Sloan and Koh, 2007). They potentially act as reservoirs for methane that could be gradually dissolved in liquid groundwater while it flows upwards to the pingo spring (Jacobsen, 2020).
There are two main pathways for methane release from lakes and ponds forming in the Arctic: Ebullition and diffusion of dissolved methane (Thompson et al., 2016; Burke et al., 2019; Jammet et al., 2017). Both could be relevant for lakes of pingos. Ebullition refers to the rapid release of bubbles containing a high concentration of methane (Peltola et al., 2017). In contrast, diffusion is a continuous process, that describes the release of dissolved methane from the lake's surface. Diffusion is thought to be more sensitive to oxidation (Thompson et al., 2016). Oxidation depicts a removal process of methane, whereby the methane is utilized as a carbon and energy source by methanotrophic microorganisms (Jiang et al., 2010).

1.4 Hypotheses

1. Reviewing relevant literature sources, there are no measurements of the spatial variability across the surface area of pingo lakes. According to field observations, LP West has no inflow from the shore areas. At the central part of the lake, it was possible to discern a point source of gas bubbling from the ground. Therefore, I expect the water to enter the lake primarily through a vent at the bottom of the lake. As the water might contain already methane when it enters the lake, I assumed that the methane concentration is the highest in the waters near the vent. At the surface, the concentration would then be in the central part near the inflow higher than at the outer parts.
Spatial variability: The position at the inflow measures a higher concentration of dissolved methane than the other positions.

2. Literature about the seasonal variability of the methane concentration in lakes of pingos is rare. During a study in 2017, the methane concentration was tracked at LP East, which is a lake that belongs to the same pingo as LP West. The methane concentrations showed a seasonal pattern with roughly three phases: a decreasing phase, a stagnating phase, and an increasing phase. The decrease was attributed to the inflow of meltwater, which diluted the methane-rich inflow from the ground (Hodson et al., 2019). After a period of stagnation, the methane concentration began to increase in August. However, the timing was uncertain as many values were interpolated. The observations led to the question of whether LP West could show a similar seasonal pattern in methane concentration.
Seasonal variability: The concentration of dissolved methane shows a seasonality, with three phases: a decreasing phase, a stagnating phase, and an increasing phase.

3. The methane flux has been solely estimated for LP East in 2017 (Hodson et al., 2019). There is no knowledge about the consistency of the fluxes over multiple years. The formation mechanism at LP is based on permafrost expansion, which is a process on time scales of decades or even centuries, see Section 2.1. The methane found in LP West potentially originates from the sub-permafrost environment and is transported in dissolved form with the groundwater to the surface. There is none, or only insignificant methane production by microbes over the summer, which could be dependent on annual variations such as the climate. Therefore, I assume a constant methane flux with regard to two years at LP West.
Annual variability: The seasonal methane flux is of a similar order in 2020 and 2021.

4. To estimate the methane flux of LP East, Hodson et al. used a diffusion model in 2019. The methane concentration used in the diffusion model was obtained through manual sampling. López Bellido et al. compared different diffusion models and chamber measurements at one lake over the summer seasons of 2009. They found higher results for the chamber measurements.
Methodic variability: The methane fluxes differ between the employed methods. The chamber measurements show higher fluxes than the diffusion model, using data from sampling or from an analyzer.

In order to test these hypotheses, I measured the concentration of dissolved methane, using two different methods: manual sampling and continuous measurements with an automatic methane analyzer in 2020 and 2021.
I estimated the methane flux using a diffusion model for 2020 and 2021. The diffusion model is based on the data of the concentration of dissolved methane. In addition, I measured environmental variables of the lake, such as the water temperature and the electrical conductivity, and weather data such as the wind speed and the air pressure. These data were as well implemented into the diffusion model.

2 Methods

2.1 Site Description

LP West is a lake that belongs to an open-system pingo, called Lagoon Pingo (LP). LP is located in the valley of Adventdalen at 78°14'26.8"N 15°45'01.1"E on the archipelago of Svalbard in the High Arctic, as shown in the left panel of Figure 2. According to the Köppen climate system, the climate in Svalbard is classified as polar tundra climate [1]. The mean annual temperature was -5.90 °C during the period of observation 1971-2000 at Svalbard Airport, around 4 km West of LP (Hanssen-Bauer et al., 2019). The permafrost at LP has an estimated depth of 22.8 m (Yoshikawa and Harada, 1995). LP West is located at the foot of the mountain Hiorthfjellet, as shown in the right panel of Figure 2. In the Southwest, there is a shallow lagoon, called Moskuslaguna, which is adjacent to the fjord Adventfjorden. The lagoon is separated from the lake through a ridge (Yoshikawa and Harada, 1995; Hodson et al., 2019).

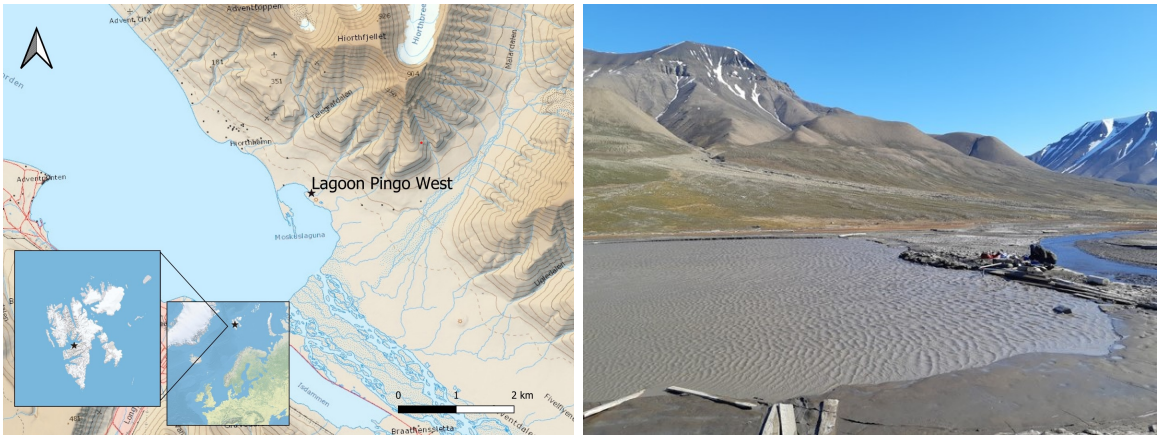

Figure 2: Left: Location of LP West in Adventfjorden on Svalbard in the high Arctic, data were downloaded from NPI (1990). Right: Terrain at LP West with the elevation of Hiorthfjellet in the background, view to the Northeast, July 2021.

From October to June, LP West is covered by ice. In the other half of the year, it features a lake of a roughly oval shape. According to field observation, there is only one inflow at LP West, which is assumed to be at the bottom of the central part of the lake. There is one outflow, located in the South. The lake has shallow banks of around 50 cm and an estimated depth of 2 m. It has a surface area of around 1475 m^2, based on graphic examinations (NPI, 2022b).
The area around LP West has a chaotic topography with a series of mounds, spanning around 500 m in length and 200 m in width. Less than 150 m eastwards of LP West, there is LP East, see the left panel of Figure 3. LP East is smaller than LP West, with a surface of around 300 m^2. During summer, it shows a drastic drop in water storage. In the right panel of Figure 3 the water level of LP East at its lowest is shown.

[1] Temperature of the warmest month greater than 0 °C but less than 10 °C (Arnfield, 2020).

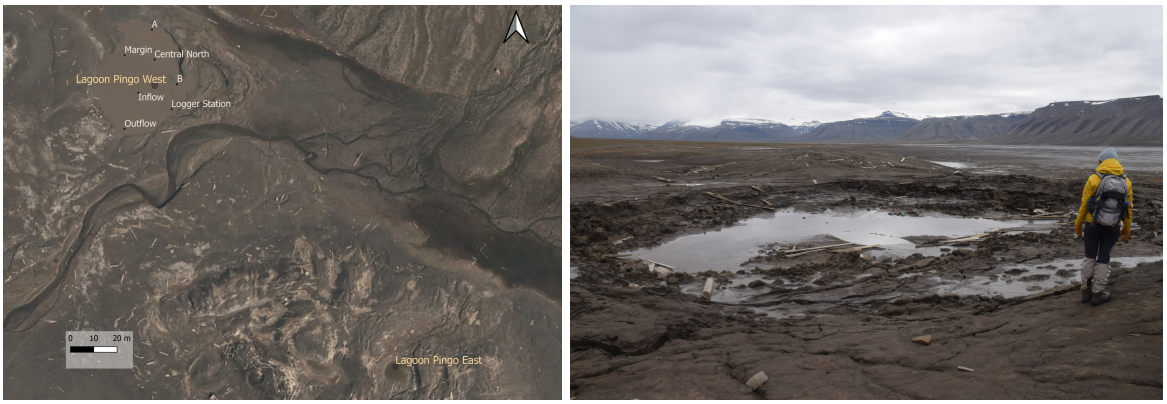

Figure 3: Left: Aerial image of LP West and LP East, labels show field work positions, data were downloaded from NPI (2022a). Right: Lake of LP East in July 2021, view to the Southeast.

The formation process of LP could follow group (c), typical for areas near the shoreline, as explained in Section 1.2. During the early Holocene, the water level of the ocean was up to 65 m higher than today (Lønne and Nemec, 2004). The uplift of the land could have resulted in a cooling of the sediments. This in turn, could have caused permafrost expansion, which forced residual water to the surface (Hornum et al., 2020). Since the hydraulic conductivity of the uplifted marine sediments of Adventfjorden is low (Hornum et al., 2020), the fluids are likely to exploit former pockmarks (Hodson et al., 2019). Pockmarks are depressions at the ocean floor created by escaping gas (Joseph, 2017). Isostatic rebound could have caused the transition of submarine pockmarks into pingo springs. The formation process, associated with group (a), seems unlikely as there are no geological faults (Hammock et al., 2022). Group (b) seems also not applicable due to a lack of warm-based glaciers dispensing meltwater (Hornum et al., 2020). Most likely, the methane in the lakes of LP originates from the sub-permafrost environment (Hodson et al., 2019), and was produced before the permafrost expansion by microbes (Jacobsen, 2020). A geogenic methane origin cannot be excluded. However, the low rates of fluid migration, that would be expected in the deeper geological sequences, might inhibit the enrichment with geogenic methane (Hodson et al., 2020).

2.2 Fieldwork

2.2.1 Environmental Variables

The environmental variables were measured with a logger station, which was set up in the central Eastern part of the lake, see the left panel of Figure 3. It could measure the water temperature in °C, electrical conductivity (EC) in mS $\cdot$ cm^{-1}, the oxidation-reduction potential (ORP) in mV, and the dissolved oxygen in mg $\cdot$ l^{-1} in one-hour steps.
Set up day was DOY 187 in 2021, and in 2020 DOY 176. Following the construction of the previous year, in 2021 the logger station consisted of three aluminum poles, one as a base frame in the ground and two for the stabilization of the sides. The connections were made using hose clamps. The left panel in Figure 4 shows the part of the construction above the water surface. The sensors were attached to the construction. These included a Campbell CS547A sensor for the lake temperature and EC, an OxyGuard-sensor for dissolved oxygen, and a Campbell CSIM11-ORP sensor for ORP. The sensors were connected through cables with the logger, a CR10 Campbell model, which was placed on the shore. The system was powered by a 12.0 V battery, shown in the right panel of Figure 4.

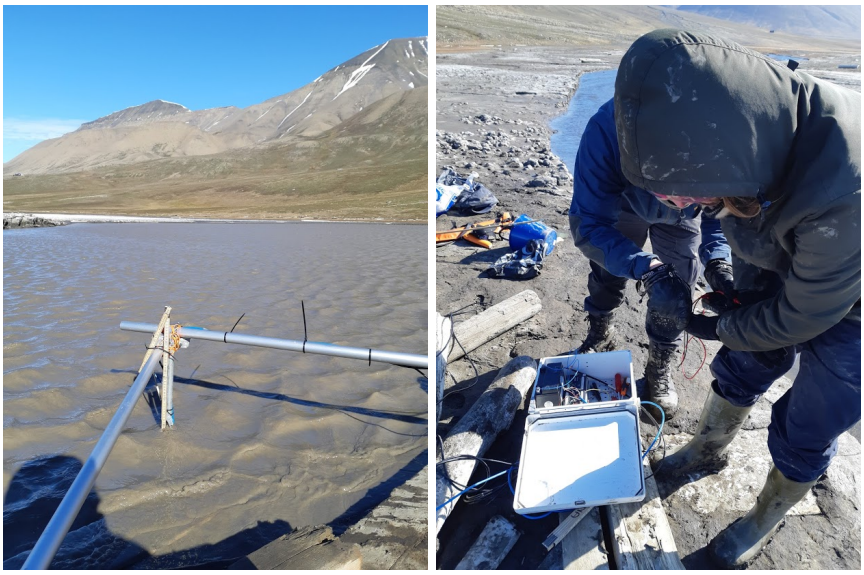

Figure 4: Left: Construction of the logger station, view to the Northwest. Right: Logger box opened, with battery and the logger, July 2021.

In 2020, the logger station featured an additional sensor, a pressure transducer, which measured the water level in cm. Due to damages in 2020, the sensor could not be reused in 2021. After the set-up, the logger station was regularly visited to check the battery and the position of the loggers. The station was removed on DOY 283 in 2021 and and DOY 254 in 2020.

2.2.2 Dissolved Methane Concentration

I measured the methane concentration in LP West using two different methods: automatically with an analyzer and manually with samples.
The automatic methane analyzer (Pro-Oceanus Digital Mini CH4) operated from DOY 222 to DOY 283 in 2021, and from DOY 177 to DOY 254 in 2020. The automatic methane analyzer is depicted in the left panel of Figure 5. It hung vertically next to the sensors at the logger station and hourly recorded the methane concentration in $mg \cdot l^{-1}$.
The manual sampling is an alternative method that was conducted in both years 2020 and 2021. A 20 ml crimp-top bottle was filled underwater and sealed with a crimper, see the equipment in the right panel of Figure 5.

Figure 5: Left: Methane analyzer from 2021. Right: Crimper and vials which were used to manually sample the methane concentration, August 2021.

In 2021, the samples were taken on 11 days between DOY 187 and DOY 274 at the position at the inflow, outflow and margin, view the left panel of Figure 3. There was another position at the central North of the lake that was neglected in further analysis, as only two samples from the beginning of the season were available. The sampling at the position at the inflow was different. It required to fill a bucket that was attached to a long stick. The vial was then filled in the bucket. In 2020, the samples were taken on 11 days between DOY 176 and DOY 267 at the position at the inflow and outflow. After the fieldwork, the samples were brought to the lab and I injected around 1 ml of 1%-NaOH solution to fix the samples. They were stored in a fridge at around 4 °C until they got transported to another laboratory and were analyzed.

2.2.3 Weather Data

The weather data were taken from an automatic weather station in Adventdalen, around 4.5 km South-Southeast from the pingo. The wind speed was measured by a Young 05103 sensor around 5 m above the ground, and the air pressure by a RM Young 61302L model, at the same height.

2.2.4 Conducting the Chamber Measurements

The chamber method was used to measure the methane flux from the water surface. I conducted the measurements in 2021 on DOY 219 from 3.13 pm to 3.22 pm and 3.30 pm to 3.36 pm, at positions "A" and "B", see the left panel of Figure 3.

The measurements were conducted using a transparent PVC chamber. The chamber had a PVC base. The base was embedded into the polystyrene platform that could float on the lake's surface, see Figure 6. Finally, the port of the chamber was connected to a hose which led to the Los Gatos Research greenhouse gas analyzer. The gas analyzer measured the methane concentration in the unit ppm, corrected for humidity and water vapor.

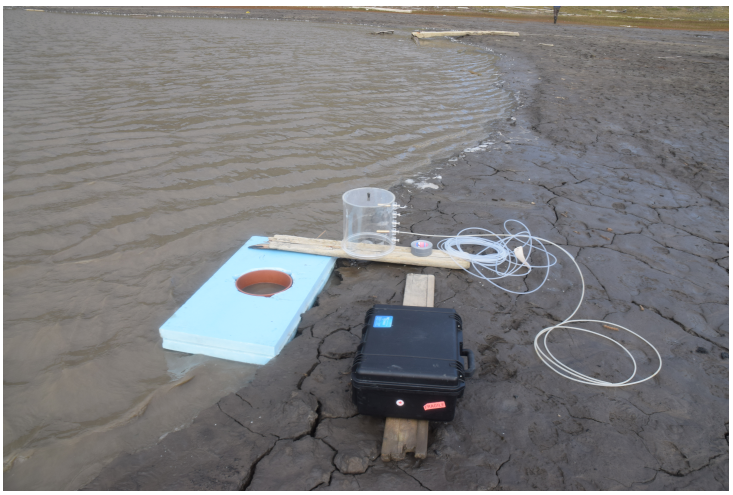

Figure 6: Equipment for the chamber measurements including the transparent PVC chamber, a polystyrene platform, a PVC base, and hoses, August 2021.

2.3 Analysis

2.3.1 Diffusion Model Set-up

I used a boundary layer diffusion model in order to estimate the diffusion flux of methane from LP West to the atmosphere for the summer seasons of 2020 and 2021 in one-hour steps.

For the flux calculations, I used Excel (Microsoft Excel, 2018), for the analysis of the model results I used R, version 2022.02.3 (RStudio, 2022).

The model is based on the concentration difference across a thin layer immediately below the air–water interface (Liss and Slater, 1974), see Equation 1. The upper boundary is in equilibrium with the atmosphere, the base equates to the concentration of the main body of the fluid. The variable k characterizes the transfer across the diffusive boundary layer, as a function of wind speed (Jansen et al., 2020). The equation is supplemented by the area A. The output of the model is the methane flux F in $mg \cdot h^{-1}$.

$$F = (C_w - C_a) \cdot A \cdot k \tag{1}$$

The flowchart in Figure 7 provides an overview of the variables in the model, including the mentioned variables for the main equation (gray), and further input variables (white), which were needed to compute the air-equilibrium concentration C_a and the gas transfer velocity k.

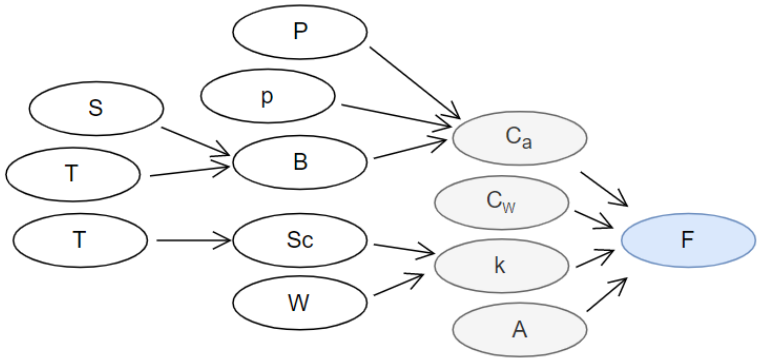

Figure 7: Overview of the diffusion model, variables represented through symbols (main variables in gray, input variables in white, the diffusion flux F in blue).

Information about the variables and associated symbols and units can be found in Table 1. Some variables were calculated, and some were directly measured.

Symbol	Variable	Unit	Type of Variable
A	Lake area	m^2	constant
C_a	Air-equilibrium concentration	$mg \cdot l^{-1}$	calculated
C_w	Methane concentration in the water	$mg \cdot l^{-1}$	measured
B	Bunsen solubility coefficient	$mg \cdot l^{-1} \cdot atm^{-1}$	calculated
k	Gas transfer velocity	$cm \cdot h^{-1}$	calculated
P	Air pressure	atm	measured
p	Partial methane pressure	$molCH_4 \cdot mol^{-1}$	constant
S	Practical Salinity Unit	No unit	measured
Sc	Schmidt number	No unit	calculated
T	Lake temperature	°C	measured
W	Wind speed	$m \cdot s^{-1}$	measured

Table 1: Information about variables for the diffusion model, in alphabetical order. Symbol; variable; unit; type of variable.

The following section explains the details of the model, defining all variables as well as specifying equations and used data. It is structured into the main variables C_a, C_w, k, and A, and their input variables.

Air-Equilibrium Concentration C_a

To start, C_a is the air-equilibrium concentration of methane. A low value of C_a compared to the actual methane concentration in the water (C_w) leads to a high flux. C_a depends on variables of the atmosphere such as the air pressure P and the partial pressure of methane in the atmosphere p, as well as a solubility coefficient B.
The formula for C_a is:

$$C_a = B \cdot p \cdot P \tag{2}$$

The variables P and p are important atmospheric variables that reflect the capacity of the atmosphere to absorb methane from the lake' surface. P is the air pressure I obtained through fieldwork measurements, see Section 2.2.3 about weather data. I converted it from mbar to atm through division by the factor 1013.25. The variable p represents the partial pressure of methane in the atmosphere. I used the partial methane pressure from Zeppelin Observatory in Ny Alesund, Svalbard, around 115 km Northwest of the fieldsite. These data were taken from: NILU (2022). I converted the unit from nmolCH_4· mol^{-1} to ppm. Missing data were calculated through linear interpolation.

The Bunsen solubility coefficient B, as used in Equation 2, represents the atmospheric equilibrium solubility of a real gas. It refers to the dynamics which occur at a lake's surface in contact with the atmosphere. The concentration of methane in the water will be in equilibrium with the partial pressure of methane in the atmosphere, expressed by the law of solubility in Equation 3, with p being the partial pressure of methane in the atmosphere, B the Bunsen solubility coefficient, and C_w the methane concentration in the water.

$$p = B \cdot C_w \tag{3}$$

B is defined as the ratio between a unit volume of gas (corrected to standard temperature 273.15 K and pressure 1 atm) and a unit volume of solvent at the measurement temperature when the partial pressure of the gas is 1 atm (Yamamoto et al., 1976).
I used the Bunsen solubility coefficient specified for methane, as suggested by Weisenburg and Guinasso in 1979. Wiesenburg and Guinassoas calculated the constants based on a data set of an experiment by Yamamoto et al. in 1975. Through this experiment, the absorption of 99.99%-pure methane into water of known salinity at several temperatures was measured. The results of the experiment were fitted to the function using the method of least squares.

The formula for the Bunsen solubility coefficient B is:

$$B = e^{(A_1+A_2\cdot\frac{100}{273.15+T}+A_3\cdot\ln(\frac{273.15+T}{100})+S\cdot(B_1+B_2\cdot\frac{273.15+T}{100}-B_3\cdot(\frac{273.15+T}{100})^2)} \tag{4}$$

The constants for methane are:
A_1=-68.8862, A_2=101,4956, A_3=28.7314,
B_1=-0.076146, B_2=0.04397, B_3=0.0068672.

I converted the unit from mlCH_4· $ml^{-1}atm^{-1}$ to molCH_4· l^{-1}· atm^{-1}, and further to mgCH_4· l^{-1}· atm^{-1} which required multiplying by the factor $\frac{273.15\cdot716}{273.15+T}$. The variable T stands for the lake temperature, which has been measured through fieldwork, see Section 2.2.1 about environmental variables.

The formula of B further incorporates S, as indicated in Equation 4. S stands for the salinity in parts per thousand, approximately equal to the Practical Salinity Unit (PSU).

This is a unit based on the properties of seawater conductivity and is required in the approach by Weisenburg and Guinasso (1979). I measured the EC in the lake, see Section 2.2.1 about environmental variables, and transformed it into the PSU, using the conversion tool on the website www.salinometry.com (2022).

Dissolved Methane Concentration C_w

C_w is the methane concentration in the upper layer of the lake in mg $\cdot$ l^{-1}. I used both the data from the samples and from the analyzer. In the case of two available samples from the same day for the same position, I used the higher value. The time of sampling was assumed to be 12.00 am for all samples. I used linear interpolation to gain values for every hour between the sampling days. Also for the analyzer methods, the gaps were linearly interpolated.

Gas Transfer Velocity k

The gas transfer velocity k impacts the methane flux, depending on the wind speed W and the Schmidt number Sc. I obtained the variable k using a quadratic function, shown in Equation 5, with a coefficient of 0.251 as suggested by Wanninkhof (2014). The coefficient was determined using remote sensing data for the wind speed (Cross-calibrated multiplatform products), the inverse modeling approach, and data on the distribution of radiocarbon provided by Sweeney et al. (2007). The coefficient was originally designed for the gas transfer velocity of carbon dioxide. It has the unit of cm$\cdot$ $h^{-1}$$\cdot$ $s^2$$\cdot$ m^{-2}. Therefore, the unit of k is cm$\cdot$ h^{-1}.

$$k = 0.251 \cdot W^2 \cdot (\frac{Sc}{660})^{-0.5} \tag{5}$$

The magnitude of methane emission changes with different wind and turbulence regimes.
The wind speed was measured through fieldwork, see Section 2.2.3 about weather data. The Schmidt number is the kinematic viscosity of the water divided by the diffusion coefficient of a gas (Wanninkhof, 2014). In the case of methane, the equation is the following:.

$$Sc = 1909.4 + (-120.78 \cdot T) + (4.1555 \cdot T^2) + (-0.080578 \cdot T^3) + (0.00065777 \cdot T^4) \tag{6}$$

In this equation, T is the lake temperature. For it, I used the results from our fieldwork, see Section 2.2.1 about environmental variables.

Area A

The area was defined as a constant value, amounting to 1475.381 m^2 based on a graphic examination of maps (NPI, 2022a).

2.3.2 Calculating the Sensitivity of the Diffusion Model

The sensitivity was calculated for the variables lake temperature, wind speed, concentration of dissolved methane, atmospheric methane concentration, atmospheric pressure, and PSU. I used the data of the models for 2020 and 2021. The flux was calculated using all measured values of the variable, that I wanted to analyze. The other variables were set to constant values amounting to the mean of the seasons of 2020 and 2021. I tested a 5.00% and 10.0% increase of the variables but did not plot these data as the differences were too low. For the variable dissolved methane concentration, I exemplarily used the values obtained through the samples. The methane flux was depicted in the unit of mg$CH_4$$\cdot$ $d^{-1}$$\cdot$ m^{-2}.

2.3.3 Analyzing the Data of the Chamber Measurements

Employing chamber measurements allowed for estimations of the methane flux from the surface of LP in the unit $mgCH_4 \cdot d^{-1} \cdot m^{-2}$. The fieldwork data represented the accumulation of methane in the chamber over time. I converted the units of the methane concentration from ppm to mol, and then mg using the ideal gas law. This reads:

$$P \cdot V = n \cdot R \cdot T \tag{7}$$

The volume V was estimated to be around 70 l, the temperature T was set at 15.4 °C according to the air temperature at 3 pm on DOY 219, and for air pressure P, I used 1000 hPa. To convert the results into the unit $molCH_4 \cdot m^{-2} \cdot s^{-1}$, I used the circular area of the chamber, estimated to be 0.07 m^2. The final transformation from mol to g required the multiplication by the molar mass of methane (16.05 $g \cdot mol^{-1}$). The unit conversions were conducted in Excel (Microsoft Excel, 2018). I extracted two passages with distinctive increases for further analysis. For the analysis, I used R. I applied a linear and an exponential regression function, the latter was designed by Dr. Claire Treat to approximate the curve of the flux. The slope of the regression curve indicated the methane flux in $\mu molCH_4 \cdot s^{-1}$ to the atmosphere.

2.3.4 Daily Flux and Seasonal Flux

The unit of the Daily Flux was $mgCH_4 \cdot m^{-2} \cdot d^{-1}$. For the diffusion model, I calculated the Daily Fluxes over the season, based on the sum of hourly fluxes, and used the mean. In the case of the chamber measurements, I scaled the results up to a daily value.
The Seasonal Flux represents the sum of hourly fluxes for a period of 100 days per square meter in the unit of $gCH_4 \cdot 100\ d \cdot m^{-2}$. As the data sets covered different time periods, the overlapping time period (DOY 187-254) was selected. The difference to 100 days, was filled with the average value per day for the number of missing days. I did not calculate Seasonal Fluxes for the results of the chamber measurements.

2.3.5 Uncertainties

For the diffusion model, I used an uncertainty of 20% for the gas transfer velocity k and 9.1% for the methane concentration C_w, as stated by Hodson et al. (2019). I used Gaussian error propagation to calculate the uncertainty for the flux based on the mean of the seasonal variables of each method. For the chamber measurements, no uncertainties were calculated.

2.4 Mapping

The maps (Figures 2 and 3) were created using the software QGis, version 3.10.06 (QGis, 2018). For the first map, the data were downloaded from the Norwegian Polar Institute (NPI, 1990). The geographical overview map features the ESRI Physical map of the Quick Map Services in QGis. For the second map, I used a WMS layer, linked to the database of the Norwegian Polar Institute (NPI, 2022a). I used the projection ETRS 89 UTM 33 (EPSG:25833).

3 Results

3.1 Dissolved Methane Concentration

The methane concentration was measured in the seasons of 2020 and 2021 using two methods: manual samples and an automatic methane analyzer.

Manual samples

In 2020, the methane concentration detected in the samples ranged from 0 to 16.6 mg· l^{-1}. The seasonal mean of 2020 amounted to 1.13 mg·l^{-1} at the inflow position, whereas the mean amounted to 0.316 mg· l^{-1} at the outflow position, see Table 2. This corresponds to a reduction by 71.7%. The standard deviation was higher than the mean for both positions. The median at the inflow position was 0.157 mg· l^{-1} and therefore lower than the value at the outflow position, where it was 0.182 mg· l^{-1}. One value for the inflow position was wide outside the range of the other measured values. This happened on DOY 176, when it measured 16.6 mg· l^{-1}. The seasonal span at the inflow position was 16.5 mg· l^{-1} in contrast to 1.58 mg· l^{-1} at the outflow position, which corresponded to a reduction by 90.4%.
In 2021, the samples showed methane concentration values ranging from 0 to 8.51 mg· l^{-1}. The seasonal mean was 2.47 mg· l^{-1} for the position at the inflow. On the other hand, the seasonal mean at the outflow position was 1.26 mg· l^{-1} and thereby 49.0% lower. Finally, the position at the margin measured a mean of 1.18 mg· l^{-1}, a value 52.2% lower than at the inflow position. The standard deviation was higher than the mean for all positions. The median of the position at the inflow was the highest among all samples, with 1.35 mg·l^{-1}. The maxima in methane concentration were ranging from 5.22 to 8.51 mg· l^{-1} for the three positions of 2021. The measured data can be found in the Appendix, see Table A2.

Parameters for the concentration of dissolved methane in mg· l^{-1} obtained through sampling						
Position	**Year**	μ	σ	**MED**	**Min.**	**Max.**
Inflow	2020	1.13	2.78	0.157	$6.40 \cdot 10^{-2}$	16.6
Outflow	2020	0.316	0.401	0.182	0	1.58
All positions	2020	0.721	1.39	0.254	$3.20 \cdot 10^{-2}$	8.23
Inflow	2021	2.47	2.72	1.35	$9.90 \cdot 10^{-4}$	8.51
Outflow	2021	1.26	1.58	0.370	$4.02 \cdot 10^{-4}$	5.30
Margin	2021	1.18	1.62	0.160	0	5.22
All positions	2021	1.64	1.79	0.491	$3.00 \cdot 10^{-4}$	5.20
Inflow	Both years	1.44	1.44	0.960	$6.38 \cdot 10^{-2}$	4.31
Outflow	Both years	0.792	0.964	0.294	$4.05 \cdot 10^{-3}$	2.92

Table 2: Statistical parameters for the methane concentration of the samples in 2020 and 2021 in $mg \cdot l^{-1}$. All positions refers to the average in methane concentration in one hour steps for all positions. Both years refers to the average in methane concentration in one hour steps for the seasons of 2020 and 2021. Position; μ mean, σ standard deviation, MED median, Min. minimum, Max. maximum.

In the early season of 2020, the methane concentration showed a significant drop at the inflow position, and a slight increase for the outflow position, as shown in the left panel of Figure 8. For both positions, there was a phase of low, stagnating values approximately between DOY 185 and DOY 215. However, no data were available between DOY 201 and 207 for the position at the outflow. After DOY 215, the concentrations increased slightly at both positions.
In 2021, the early season showed slightly rising concentrations, approximately until DOY 195. In the following period the methane concentration showed stable values close to zero. After DOY 228 the concentrations increased. A peak arose at the inflow position on DOY 240 amounting to 8.51 mg· l^{-1}. At the outflow position a peak occurred on DOY 254 with a lower concentration of 5.30 mg· l^{-1}, synchronically with the position at the margin with 5.22 mg· l^{-1}.

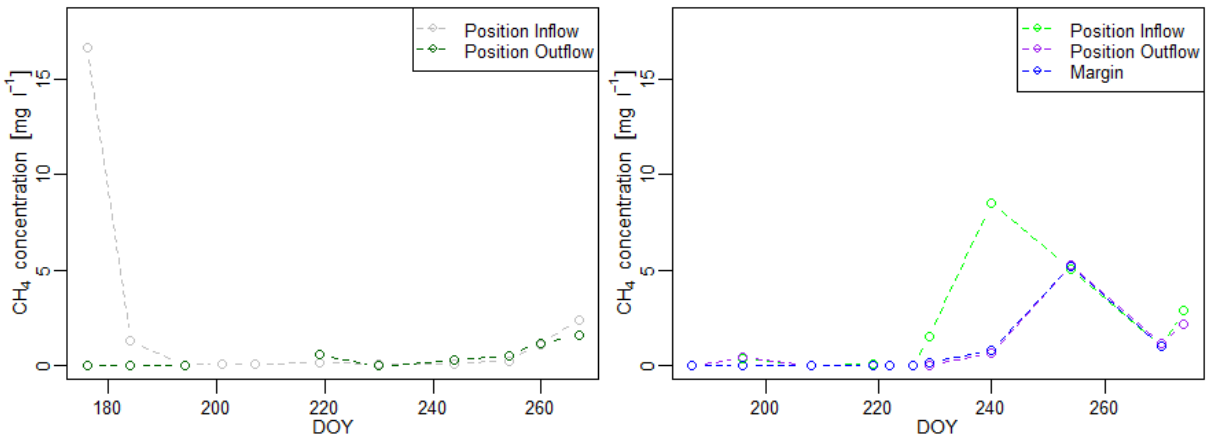

Figure 8: Left: Methane concentration in $mg \cdot l^{-1}$ for the position at the inflow and outflow in 2020. Right: Methane concentration for the position at the inflow, outflow and margin in 2021.

Automatic Analyzer

Figure 9 shows the methane concentration in mg· l^{-1} over the summer seasons of 2020 and 2021 in one-hour time-steps. In 2020, the concentration rose in the early season from values close to 0 to 3.61 mg· l^{-1} at 9 am of the DOY 183. The following period could not be monitored. The data after DOY 220 showed periodic increases and decreases. The concentration peaked again on DOY 236, 9 am, amounting to 4.44 mg· l^{-1}. The mean was 2.01 ± 0.70 mg· l^{-1}.
In 2021, the analyzer monitored the methane concentration at the same position. The data encompass only the period after DOY 220. The concentration showed a positive trend with increasing short-term variabilities. The maximum was on DOY 259 at 1 am amounting 10.4 mg· l^{-1}, followed a few days later by the minimum on DOY 272, 3 am, with 0.113 mg·l^{-1}. The mean concentration measured by the analyzer during 2021 was 3.12 ± 1.91 mg· l^{-1}.

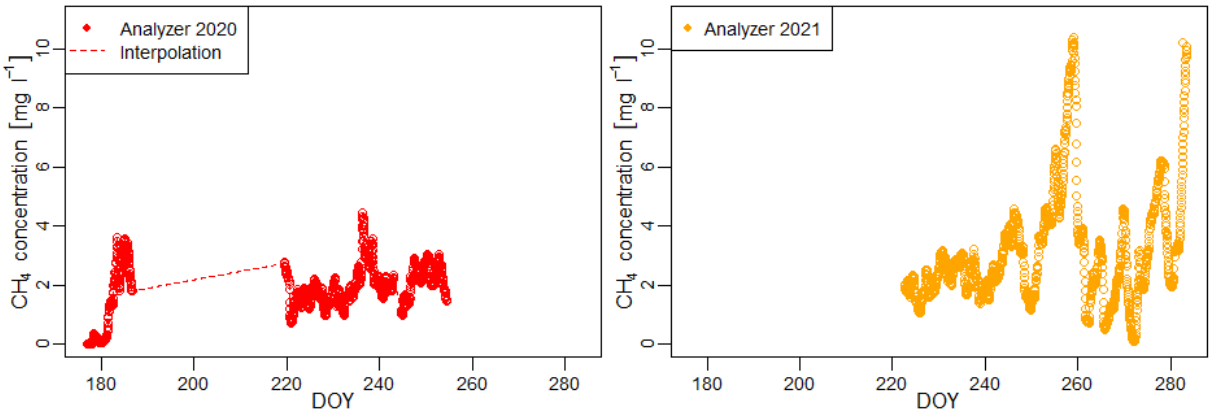

Figure 9: Left: Methane concentration in $mg \cdot l^{-1}$ in LP West measured through an analyzer in 2020. Right: Equivalent data as in the left panel but for 2021.

3.2 Methane Flux Obtained with the Diffusion Model

The methane fluxes, in the unit of $mgCH_4 \cdot m^{-2} \cdot d^{-1}$, also referred to as Daily Fluxes, were calculated for the summer seasons of 2020 and 2021. In 2020, the data accounted for the position at the inflow and outflow, see Figure 10. The Mean Daily Flux for the position at the inflow in 2020 was 56.8 ± 12.8 $mgCH_4 \cdot m^{-2} \cdot d^{-1}$. The uncertainty was calculated as explained in Section 2.3.5. The median was 4.46 $mgCH_4 \cdot m^{-2} \cdot d^{-1}$. For the position at the outflow the mean amounted to 6.29 ± 5.59 $mgCH_4 \cdot m^{-2} \cdot d^{-1}$, whereas the median was 2.03 $mgCH_4 \cdot m^{-2} \cdot d^{-1}$.

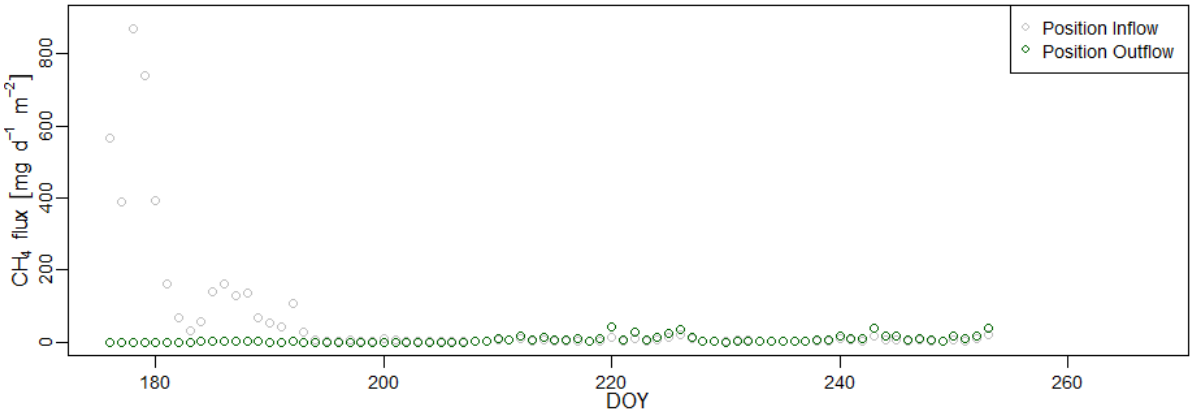

Figure 10: Daily Flux in $mgCH_4 \cdot m^{-2} \cdot d^{-1}$ from the lake's surface based on the sample concentration for each position in 2020.

In 2021, the Daily Fluxes for the three positions were similar in terms of the pattern even though value ranges differed in magnitude, see Figure 11. The patterns indicated a characteristic increase in methane fluxes at the end of August and September. The Mean Daily Flux at the inflow position was 141 ± 40 $mgCH_4 \cdot m^{-2} \cdot d^{-1}$. The mean for the position at the outflow was 83.9 ± 20.9 $mgCH_4 \cdot m^{-2} \cdot d^{-1}$. For the position at the margin, the mean was 74.1 ± 19.6 $mgCH_4 \cdot m^{-2} \cdot d^{-1}$. The medians were significantly lower with 34.0, 23.1, and 3.05 $mgCH_4 \cdot m^{-2} \cdot d^{-1}$ respectively.

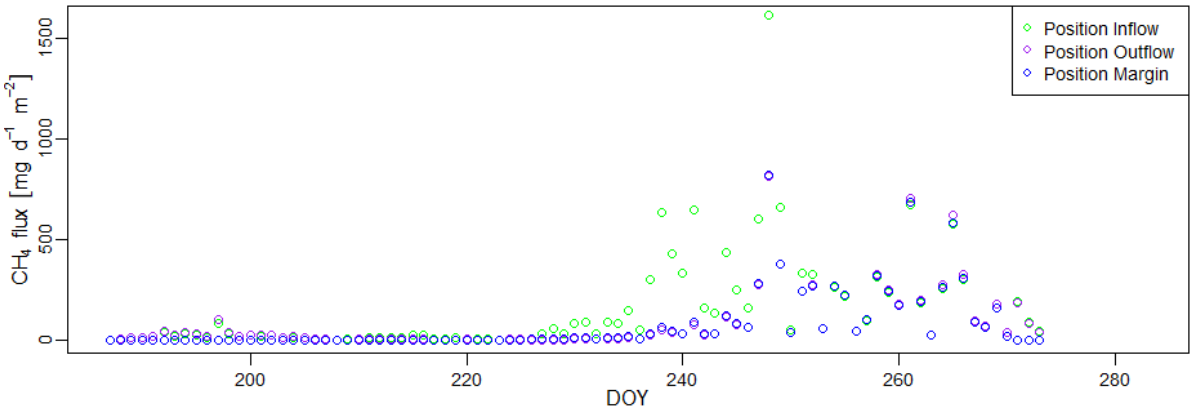

Figure 11: Daily Fluxes in $mgCH_4 \cdot m^{-2} \cdot d^{-1}$ from the lake's surface based on the sample concentration for each position in 2021.

The Daily Fluxes based on the analyzer method, are shown in Figure 12. The fluxes in 2020 had a mean of 98.7 $mgCH_4 \cdot m^{-2} \cdot d^{-1}$. The median was 70.0 $mgCH_4 \cdot m^{-2} \cdot d^{-1}$. In 2021, the analyzer had a mean of 211± 51 $mgCH_4 \cdot m^{-2} \cdot d^{-1}$, and the median was 121 $mgCH_4 \cdot m^{-2} \cdot d^{-1}$. The maximum value was 1444 $mgCH_4 \cdot m^{-2} \cdot d^{-1}$ on DOY 277.

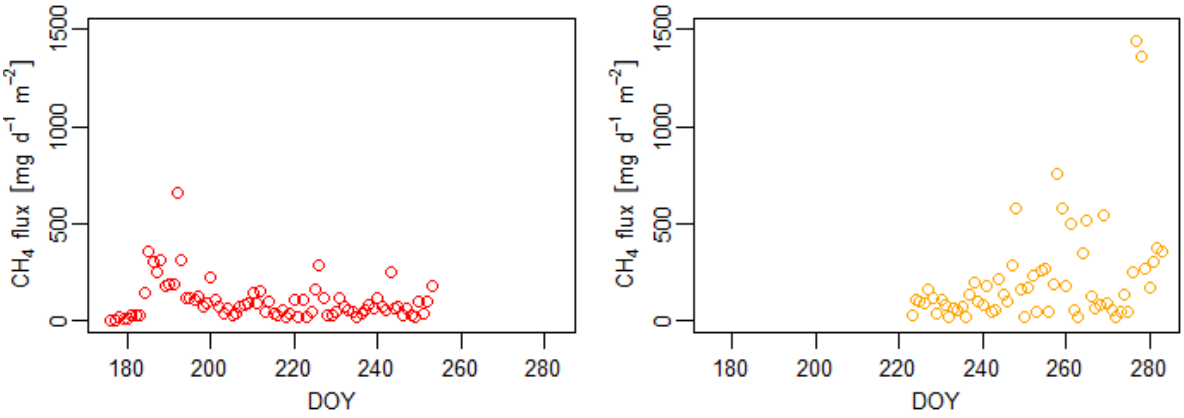

Figure 12: Left: Daily Fluxes in $mgCH_4 \cdot m^{-2} \cdot d^{-1}$ from LP West based on measurements of an automatic methane analyzer in 2020. Right: Equivalent data as in the left panel but for 2021.

3.3 Methane Flux Obtained with the Chamber Measurements

In 2021, I could apply the chamber method on DOY 219 between 3.13 to 3.22 pm at position A near the logger station. Figure A7 in the Appendix shows the methane concentration for 557 seconds. The slope of the linear regression was $7.08 \cdot 10^{-3}$ ppm $\cdot$ s^{-1}, and that of the exponential regression was $12.9 \cdot 10^{-3}$ ppm $\cdot$ s^{-1}. According to the results of the linear regression, the flux value was 173 $mgCH_4 \cdot m^{-2} \cdot d^{-1}$. According to the exponential regression instead, the value was 316 $mgCH_4 \cdot m^{-2} \cdot d^{-1}$. The sum of squared residuals indicated a better fit for the linear regression with 6419, than for the exponential regression with 16952.
For position B, the data series of methane concentration over time was taken between 3.30 pm to 3.36 pm. The plot of the concentration in ppm $\cdot$ s^{-1} covers 377 seconds, see Figure A8 in the Appendix. The steepest increase of the methane concentration can be seen after approximately 100 s. As for position A, I performed linear and exponential regression. The linear slope was $4.84 \cdot 10^{-3}$ ppm $\cdot s^{-1}$, while the exponential slope was $6.80 \cdot 10^{-3}$ ppm $\cdot s^{-1}$. According to the results of the linear regression, the flux was 119 $mgCH_4 \cdot m^{-2} \cdot d^{-1}$. According to the exponential regression, the flux was higher, amounting to 166 $mgCH_4 \cdot m^{-2} \cdot d^{-1}$. The linear regression showed a similar sum of squared residuals as the exponential regression (2264 vs. 2284).
The linear regression method resulted in a difference of 55.0 $mgCH_4 \cdot m^{-2} \cdot d^{-1}$ between the position A and B. The flux at position A, closer to the inflow, was higher. Using the exponential regression method, the difference was even more enhanced, being 150 $mgCH_4 \cdot m^{-2} \cdot d^{-1}$. The flux at position A was also higher with this method.

3.4 Comparison of Fluxes

The flux estimations showed to depend on the method, the position, and the year, see Table 3. In 2021, the chamber measurements at position A processed with exponential regression yielded the highest Daily Flux with 316 $mgCH_4 \cdot m^{-2} \cdot d^{-1}$. The regression method played a significant role. The fluxes of the chamber measurements using linear regression were 28.5% lower compared to those using exponential regression, for position A, and 45.0% lower for position B. However, the results of the linear regression had a lower sum of residual squares than those of the exponential regression at position A. For position B the sum of residual squares was similar for the results of both regression types.
The Mean Daily Flux derived from the analyzer in 2021 was 211 $mgCH_4 \cdot m^{-2} \cdot d^{-1}$ and therefore higher than the results of the chamber measurements. An exception was found for the chamber measurements at position A using exponential regression.

As the chamber measurements were conducted only for a few minutes on one day, the fluxes can be compared for the duration of one hour in the unit of $mgCH_4 \cdot m^{-2} \cdot h^{-1}$ to the ones from the diffusion model. Thereby, I compared position A with the inflow position, as it was the nearest, and position B, with the margin position. The diffusion model indicated a flux of 0.428 $mgCH_4 \cdot m^{-2} \cdot h^{-1}$ for 3 pm on DOY 219 for the inflow position, whereas the chamber measurements indicated 7.40 $mgCH_4 \cdot m^{-2} \cdot h^{-1}$ or rather 13.5 $mgCH_4 \cdot m^{-2} \cdot h^{-1}$ at position A for linear and exponential regression, respectively. The diffusion model at the margin position, close to position B, recorded a flux of $8.56 \cdot 10^{-3}$ $mgCH_4 \cdot m^{-2} \cdot h^{-1}$ compared to 5.08 $mgCH_4 \cdot m^{-2} \cdot h^{-1}$ or rather 7.11 $mgCH_4 \cdot m^{-2} \cdot h^{-1}$ for the chamber measurements, for linear and exponential regression, respectively. The analyzer did not provide any data for DOY 219.
The diffusion model based on sampling showed the lowest fluxes in 2020 and 2021. Those fluxes showed large differences depending on the position. The position at the inflow had the highest mean in both years. The flux at the inflow was 9.03 times higher than that at the outflow in 2020. In 2021, the flux at the inflow was 1.68 times higher than that at the outflow. In 2021, the position at the margin had the lowest flux value with 74.1 $mgCH_4 \cdot m^{-2} \cdot d^{-1}$.
The Mean Daily Fluxes showed higher values in 2021 than in 2020. The position at the inflow recorded an increase of 149% from 2020 to 2021, and the position at the outflow an increase of 1234%. According to the analyzer method, the flux increased by 114%.
The Seasonal Flux amounted to 1.69 $gCH_4 \cdot 100\ d \cdot m^{-2}$ in 2020 for the average of the positions and to 8.17 $gCH_4 \cdot 100\ d \cdot m^{-2}$ in 2021. This corresponds to an increase of 383%.

Method	**Year**	**Position**	**(Mean) Daily Flux** in $mgCH_4 \cdot m^{-2} \cdot d^{-1}$	**Uncertainty** in $mgCH_4 \cdot m^{-2} \cdot d^{-1}$
Diffusion model Sampling	2020	Inflow	56.8	12.8
Diffusion model Sampling	2020	Outflow	6.29	5.59
Diffusion Model Sampling	2020	Average of positions	31.5	8.2
Diffusion model Sampling	2021	Inflow	141	40
Diffusion model Sampling	2021	Outflow	83.8	20.9
Diffusion model Sampling	2021	Margin	74.1	19.6
Diffusion model Sampling	2021	Average of positions	99.8	27.1
Diffusion model Analyzer	2020	Logger station	98.7	22.8
Diffusion model Analyzer	2021	Logger station	211	51
Chambers Lin. Regression	2021	A	173	–
Chambers Exp. Regression	2021	A	316	–
Chambers Lin. Regression	2021	B	119	–
Chambers Exp. Regression	2021	B	166	–

Table 3: Mean Daily Fluxes in the unit of $mgCH_4 \cdot m^{-2} \cdot d^{-1}$ for the diffusion model, and Daily Fluxes for the chamber measurements, scaled up from values in the unit of $mgCH_4 \cdot m^{-2} \cdot s^{-1}$. The uncertainty for the diffusion model was based on the uncertainties for the gas transfer velocity k, 20%, and for the dissolved methane concentration, C_w 9.1%, according to Hodson et al. 2019. For the chamber method uncertainties were not calculated.

3.5 Main Results

1. In 2020, the methane concentration showed the highest seasonal mean with 1.13 $mg \cdot l^{-1}$ for the inflow position. The methane concentration at the position at the outflow was 71.7% lower. In 2021, the concentration was 2.47 $mg \cdot l^{-1}$ at the inflow position, whereas the concentration measured at the outflow was 49.0% lower and at the margin 52.2% lower than at the inflow.
2. In the early season of 2020, only the position at the inflow showed a drop in methane concentration. The outflow position did not reflect this decreasing pattern. The following period showed low, nearly constant values. Afterward, in 2020 the concentration increased slightly for the samples. In 2021, the concentration of dissolved methane did not show a decrease at the beginning of the season. The pattern showed a slight increase. There was a steep increase starting on DOY 229. However, the data showed a decline after DOY 240 at the inflow position and after DOY 254 at the other positions.
3. The Mean Daily Flux for the position at the inflow in 2021 was 149% higher compared to the same position in 2020. The position at the outflow showed an increase of 1234% from 2020 to 2021. The average of the positions showed an increase of 216% from 2020 to 2021. According to the analyzer method, the flux increased by 114% from 2020 to 2021. The Seasonal Flux increased by 383% for the average of the positions from 2020 to 2021.
4. The diffusion model, using the analyzer method, yielded the highest methane fluxes, except for the chamber measurements using exponential regression at position A. The diffusion model, based on samples, yielded the lowest fluxes.

4 Discussion

4.1 Dissolved Methane Concentration

4.1.1 Spatial Variability

Hypothesis: The position at the inflow measures a higher concentration of dissolved methane than the other positions.

The concentration of dissolved methane showed an unequal distribution across the lake's surface, dominated by the position near the inflow. The seasonal mean of the position at the inflow was 2–3.5 times higher than the means of the other positions encompassing the margin and outflow, see Table 2. Thompson et al. (2016) suggested that spatial variabilities in the methane concentration in Arctic lakes result from processes, which control methane cycling, such as methane production, consumption, and transport.

First, I will discuss methane production as a possible reason for the observed spatial variability at LP West. During the summer season of 2021, I could observe bubbles frequently escaping from the ground in the central part of the lake. These bubbles might be an indicator of the inflow of groundwater. The groundwater at LP originates from the subpermafrost environment (Hornum, 2018; Hodson et al., 2020; Hornum et al., 2020), and might transport dissolved methane into the lake. At LP East, Hodson et al. discerned a point in the center of the lake, where they suspected the water inflow would be, described as a vertical shaft of around 0.5 m in diameter (Hodson et al., 2019).

Given the bubbling and the high concentration of methane in the central part of LP West, the inflow of groundwater, transporting methane into the lake, is likely. If there was another dominant source of methane at LP West, the spatial variability would differ from the observed pattern. Toolik lake in Alaska shows the reversed distribution of methane across the lake's surface, with high methane concentrations at the margins and low concentrations at the center. It receives its water mainly through two rivers entering the lake at the margins (Lecher et al., 2017). The rivers are fed by subterranean groundwater enriched with methane. This methane is produced through microbial activity in the active layer of the watershed belonging to Toolik lake (Lecher et al., 2015). At LP West, there are no indications of surface streams entering the lake. Moreover, the shallow permafrost and active layer of the wetlands in the valley show low methane concentrations at many positions, especially in areas with low water saturation and low organic carbon content (Jones, 2019). In the future, the watershed of LP West could be further analyzed in terms of organic carbon content, methane concentration, and microbial composition to estimate the potential of terrestrial methane sources entering LP West.

A similar spatial variability in methane concentration with high concentrations at the margins was observed at a small lake near Kangerlussuaq in Greenland (Thompson et al., 2016). This lake is mainly fed by melting snowpack and direct precipitation. The underlying process was methanogenesis in the bottom sediments, with increased productivity in the sediments near the shore, where the microbes found a greater amount of recently deposited labile organic material (Thompson et al., 2016; Phelps et al., 1998). At LP West, it is not clear whether methanogenesis occurs in the bottom sediments. At LP East, the general conditions in the sediments would be conducive for methanogenesis (Hodson et al., 2019). However, methane production normally commences after reservoirs of alternative electron acceptors are depleted (Achtnich et al., 1995; Capone and Kiene, 1988). As a consequence, the activity of microorganisms other than methanogens may outcompete methanogenesis, for example in substrate limited areas with an abundance of sulfate (Delaune et al., 1983). At LP East, the sulfate concentration amounted to 103 ± 11 mg$\cdot$ l^{-1} in the summer season of 2017. Black sulfide precipitates and the odor of hydrogen sulfide indicated the reduction of sulfates (Hodson et al., 2019). The reduction of sulfate could diminish the methane production in the sediments at LP West.

Conclusions about sulfate reduction could be obtained by looking at the ORP and the content of sulfate in LP West.

The transport of methane to the surface and outer parts of the lake depends on mixing. Convection is one of the main processes controlling mixing in lakes. It refers to motions that result from the action of gravity upon an unstable density distribution in a fluid (Bouffard and Wuest, 2019). In winter or spring, density instabilities might occur in ice-covered lakes when the insulating snow layer on the ice vanishes and solar radiation penetrates the ice layer (Kirillin et al., 2018; Mironov et al., 2002). The water on the underside of the ice layer might become denser than the water below and convection might be induced transferring stored gases to the surface (Eugster et al., 2003; Bengtsson, 1996). Kirillin et al. (2012) argue that convection depends on salt distribution. Stratification caused by salts, for example through sediments enriching the near-bottom water with salts, could suppress convection. This aspect could be relevant for LP West as the sediments are known to be salty due to their marine origin (Hodson et al., 2019), and the meltwater inflow could cause the formation of an upper water layer with low salt concentrations. However, there are no data about the stratification at LP West and the implications on convectional mixing and on the distribution of the methane concentration.
Moreover, variations in the ice and snow thickness, and depth differences between shallow and deep parts of the lakes could cause lateral temperature gradients and initiate horizontal convection (Kirillin et al., 2012; Farmer, 1975; Cortés and Macintyre, 2019). At LP West, neither the occurrence of mixing through vertical convection nor convection in the horizontal dimension is proven. Furthermore, it is questionable whether convection below the ice cover would be able to impact the spatial variability found in methane concentrations in the open water after ice thaw. Convection in summer and autumn might be associated with density instabilities due to surface cooling and heavy rainfall (Jansen et al., 2020; Kirillin et al., 2012). In addition to convection, turbulence, e.g. from wind shear, could moderate mixing within the water column (Hodson et al., 2019). At LP West, the highest seasonal methane concentration was found on DOY 176 in 2020 amounting to 16.6 mg$\cdot$ l^{-1}, and DOY 240 in 2021 amounting to 8.51 mg$\cdot$ l^{-1}. Both were measured at the inflow position. In 2020, the wind speed showed low to medium values, not higher than 7.40 m$\cdot$ s^{-1} in the period of three days before the maximum in methane concentration, as measured at Adventdalen weather station. In 2021, the wind speed showed a rise up to 10.5 m$\cdot$ s^{-1} in the period of three days before the maximum in methane concentration (Norsk Klimaservicesenter, 2022). There was no observed correlation between the methane concentration and the wind speed. However, it could be that high wind speeds cause short-term increases in dissolved methane at the inflow position due to the up-welling of methane from the deeper water column, and in the following hours lateral mixing, leading to decreased spatial variabilities. Also, the wind direction could affect the methane concentrations measured at different positions at the lake, as persistent wind from one direction could result in the accumulation of dissolved methane at the shore of the downwind side of the lake. Furthermore, the sheltering due to the elevation of LP East and the mountainside could impact the spatial variabilities at LP West.
An indicator of mixing could be the lake color of LP West. The color was on some days less transparent than on others, which could indicate dispersing of particles. Another indicator of mixing could be the spatial variability of the pattern of methane concentration detected in the late season in 2021. At first, the position at the inflow showed a maximum concentration of dissolved methane. The other positions showed maximum concentrations 14 days later, reaching almost the level of the position at the inflow. It could be that the methane originates from the inflow position, and is mixed up in a process of several days with the water in other parts of the lake.
Additional measurements at more positions around the inflow would help to determine the concentration gradient and mixing rate between the inflow and other positions.

4.1.2 Seasonal Variability

Hypothesis: The concentration of dissolved methane shows a seasonality, with three phases: a decreasing phase, a stagnating phase, and an increasing phase.

During the early season in 2020, the position at the inflow showed a drop-down in methane concentration. However, concentrations detected in the samples of the position at the outflow and all samples of 2021 did not show a decreasing pattern. Also, the analyzer did not show a decreasing pattern.
As explained in the 2. Hypothesis in Section 1.4, I expected a decrease in the methane concentration due to the inflow of meltwater, which contains no or only little methane (Hodson et al., 2019). Measurements of the EC could answer the question of whether meltwater diluted the lake and when that occurred. Meltwater is expected to have a lower EC than groundwater. Therefore, the inflow of meltwater would manifest in a decrease in the EC in the lake (Hodson et al., 2019).
In both years, 2020 and 2021, the EC showed a steep increase of approximately 2–3 $\mathrm{mS} \cdot \mathrm{cm}^{-1}$ at the beginning of the season, followed by a gradual increase and constant passages, see Figure A3 in the Appendix. There was no decrease in the EC, as it was expected when meltwater enters the lake. However, a decrease in the EC could have happened before the start of the measurements. The measurements of the EC started on DOY 176 in 2020 and DOY 187 in 2021. At that time, most of the snow and ice had already melted. The observed increase in the EC could point toward a decline in the proportion of meltwater in the lake (Hodson et al., 2019). It has been observed at other lakes in the Arctic that the EC showed an increase for a few days or weeks due to the reduced inflow of meltwater (Cortés and Macintyre, 2019; Szczucińska, 2011). Future measurements of the EC could start earlier in the season, to retrace the assumed correlation between the EC and the meltwater inflow. This could contribute to the understanding of the impacts of meltwater inflow on methane concentration during the early season.
The water level could be another proxy for the inflow of meltwater. In 2020, the water level showed nearly constant values in the early season, see Figure A4 in the Appendix. It is not clear whether there was no meltwater inflow, or the data do not reflect the inflow of meltwater. The latter could be the case, because of measurement errors. The sensor could have been not well calibrated. It could also be that the water level is not correlated with the inflow of meltwater because of changes in the outflow rate. The outflow could increase as soon as meltwater enters the lake. Therefore, the water level could remain constant, while the methane concentration would decrease. In contrast, the water level decreased at LP East over the summer season of 2017 (Hodson et al., 2019). Further measurements of the water level and the outflow are needed to find out whether there is no significant meltwater inflow or the water level is just not correlated with the inflow of meltwater at LP West. These measurements could help to understand the response of the methane concentration to the inflow of meltwater.

The thaw of the ice cover in spring could lead to a decrease in the methane concentration, which could have happened before the start of sampling and could explain the low methane concentration found in most of the samples in June and July.
Ice acts as a barrier to atmospheric exchange (Ricão Canelhas et al., 2016; Striegl et al., 2001). Therefore, an ice cover might enable the accumulation of methane during wintertime (Greene et al., 2014; Denfeld et al., 2016). When the ice cover thaws, accumulated methane might escape. Hence, the methane concentration would show a decrease.
For LP West, no data on the methane concentration below the ice cover were available. At LP East, ice drilling enabled to obtain data on the methane concentration in April 2016 and 2017. In 2016, the concentration amounted to 14.5 $\mathrm{mg} \cdot \mathrm{l}^{-1}$, and in 2017 to 9.63 $\mathrm{mg} \cdot \mathrm{l}^{-1}$ (Hodson et al., 2019).

These values are higher than any value measured when the water was not covered by ice, which could indicate the accumulation of methane due to the ice cover. At LP West, the possibility of methane accumulating beneath the ice cover could be further investigated.
During the melting phase in June, I observed the abundance of fissures, puddles, and streams of meltwater at LP West. Fissures occurring in the ice cover might enable the release of methane (Ricão Canelhas et al., 2016). Potentially, the level of methane could already drop when the first fissures occur. An early or rapid decrease would prevent that I see any decrease due to the inflow of meltwater, which would be more gradual.
When the lake exhibited open water, none of the samples measured a methane concentration higher than 0.500 mg$\cdot$ l^{-1} in June, except for the inflow position of 2020. At LP East, there were only interpolated data for June. The actual values could have been even lower, given that there were very low concentrations in July. These data reinforced the statement that the early season is characterized by low methane concentrations.
A study on taiga lakes in 1995 and 1996 in Alaska monitored the timing of methane releases from reservoirs beneath the lake ice in spring. The study emphasized that methane outbursts take typically only a few days, and the onset of the outburst can be earlier and the duration shorter directly near the shore (Phelps et al., 1998).
In Northern Sweden, the monitoring of an ice-covered lake in 2013 showed that irregular melting across the surface enabled multiple, phased outbursts, instead of a unique outburst (Jammet et al., 2015).
Also at LP West, out-gassing could cause high fluctuations in the methane concentration during the early season. Chamber measurements could be useful to capture methane fluxes during the period of the ice break-up and solve the question of whether out-gassing occurred before sampling started or the concentrations persisted at low levels.
Furthermore, the seasonal variability in methanotrophy could influence the methane concentration. The presence of an ice lit inhibits the input of atmospheric oxygen. Less oxygen in the water column reduces the potential for methanotrophy (Jammet et al., 2017). Hence, the methane concentration would be higher in the period of ice cover and decrease with the ice break-up. The data about oxygen content in LP West started after the thaw of the ice cover. Therefore, it is not possible to draw conclusions about the oxygen depletion under the ice lit. At LP East, extractions below the ice lit in March and April 2017 showed oxygen concentrations between 1.71 and 2.44 mg$\cdot$ l^{-1}. The actual concentrations could have been even lower because of the contamination of the samples with oxygen after the extraction (Hodson et al., 2019). Carbon isotope analysis at LP East pointed toward oxidation under the ice cover during the winter season (Hodson et al., 2019).
At LP West, the hourly mean oxygen concentrations in July 2020 amounted to 5.10 mg$\cdot$ l^{-1} in 2020, and 8.62 mg$\cdot$ l^{-1} in July 2021, see Figure A2 in the Appendix. It could be that the input of oxygen into the lake increases the rate of methanotrophy in the early summer season. However, the present data do not allow the recognition of a correlation between oxygen and methane at LP West.
Furthermore, methanotrophy could be limited by temperature. Phelps et al. (1998) assumed that methanotrophy is generally inhibited in cold waters. However, Ricão Canelhas et al. (2016) found oxidized methane at temperatures as low as 2 °C. Methanotrophy is also sensitive to the trophic status of the lake which could change with the presence of an ice cover (Sepulveda-Jauregui et al., 2015). Further analysis of the conditions in the water enabling methanotrophy could be useful to understand and predict the methane concentrations in the early summer season at LP West.
In July, the concentration of dissolved methane showed values close to 0 mg$\cdot$ l^{-1} in both years at LP West. This overlaps with the assumption of a stagnating phase after the melting period. In comparison, LP East showed methane concentrations of $5.00 \cdot 10^{-3}$ mg$\cdot$ l^{-1} in the two samples of July 2017 (Hodson et al., 2019).

Methanotrophy could have continued during that period, causing low methane concentrations, as suggested by Hodson et al. (2019) for LP East.
In the last phase of the season, the concentration showed a slight increase for the samples of 2020, and an even steeper increase for the samples of 2021, which declined after 10–20 days.
The declines, detected in the samples of 2021, could not be representative of the late season, and rather originate from isolated lows, that were part of high fluctuations. The analyzer indicated high, daily fluctuations towards the end of the season of 2021. Also, the methane concentration observed at LP East in 2017, showed stronger, hourly to daily variations in the late season. A possible explanation is the reduced impact of the hydrological forcing, which caused rather slow and gradual changes, and the increased impact of the meteorological forcing, with hourly to daily variations (Hodson et al., 2019). This mechanism could be relevant for LP West in the late summer season and cause high fluctuations.
The observed peak in the methane concentration measured by the analyzer on DOY 283 in 2021 could depict an autumn outburst, as observed in many lakes (López Bellido et al., 2009; Kankaala et al., 2006; Riera et al., 2011). During a study in 2002 on a small, boreal lake in Finland, it was observed that the autumn outburst followed the upwelling of water from the hypolimnion to the surface. Before the upwelling, the methane concentration had reached very high levels in the hypolimnion, greater than in any other period of the season. The upwelling itself was a process of short duration leading to a very intense methane outburst at the surface (Kankaala et al., 2006). At LP West, it is not known whether the water stratifies over the summer and methane can accumulate in deeper layers. Sampling or measurements of the methane concentration and water temperature at different water depths could solve this question and indicate whether upwelling could cause intense outbursts in the late season.

During the entire season, daily to monthly changes in the inflow rate could have deformed the expected seasonal pattern in methane concentration. At both LP West and LP East, there are no data about the inflow rate. However, in LP East the inflow rate is assumed to vary. In August 2017, the water level showed an increase, which could not be attributed to precipitation (Hodson et al., 2019). Hence, the increase in water level could have been a result of the increased inflow. Changes in the methane source in the groundwater would be possible as well. There are no data on seasonal variations in the methane source at LP West. Monitoring at LP East showed that the proportion of thermogenic methane and biogenic methane detected in the samples of 2017 potentially varied. During ice cover, the isotope composition of methane indicated a greater proportion of thermogenic methane (Hodson et al., 2019). At LP West, an additional supply of methane or the reduction of the supply could be possible as well.
The hypothesis was derived from observations about the seasonal methane concentration at LP East in 2017. The seasonal pattern in methane concentration at LP West could be different from LP East. The onset of the thaw of the ice cover could be different, depending on the different diameter and curvature of the ice lid, the exposure to wind, and the removal of insulating snow. Moreover, the varying depth of the active layer and the availability of dissolved salts (Hammock et al., 2022), could contribute to different seasonal patterns in methane concentration found at both lakes. So far, monitoring was not conducted at both lakes in the same year. Data for both lakes in the same year would enable to refine estimations about the seasonal variability at LP West and LP East.
In general, seasonal variability in methane concentrations in many aquatic systems is known to primarily depend on methanogenic activity, coinciding with factors such as the soil or sediment temperature and plant productivity (Kankaala et al., 2006; Nat and Middelburg, 1998; Werner et al., 2003). In contrast, LP West could depend more on methanotrophic activity and the hydrological and meteorological forcing.

4.2 Methane Flux

4.2.1 Annual Variability

Hypothesis: The seasonal methane flux is of a similar order in 2020 and 2021.

Comparing the Mean Daily Flux for the average concentration of the positions revealed a higher flux in 2021, with an increase of 216%. The Seasonal Flux in a period of 100 days, even revealed an increase of 383% from 2020 to 2021, based on the average of the sample positions in each year. The results raised doubts about the assumed consistency of methane fluxes throughout time periods of years.

In general, the temporal patterns in methane fluxes track the temporal patterns in methane concentrations (Loken et al., 2019). At LP West, the mean methane concentration in 2021 exceeded for each position the mean of 2020: For the position at the inflow the annual increase amounted to 119% and for the position at the outflow the increase amounted to 294%. This could partly explain the annual increases in the Mean Daily Fluxes which amounted to 149% for the inflow and 1234% for the outflow.

The added variability in flux can be attributed to variations in wind speeds (Loken et al., 2019). However, the mean wind speed was in 2020 higher than in 2021. The hourly mean amounted to 5.17 ± 2.97 $m \cdot s^{-1}$ between June and September of 2020, and 4.86 ± 2.54 $m \cdot s^{-1}$ in 2021, as measured in Adventdalen (Norsk Klimaservicesenter, 2022). Hence, the wind speed is not a likely cause of the annual variability detected in this study.

The fluxes covered a later period in 2021 than in 2020. The underlying seasonal variabilities in the different periods could contribute to the higher Daily Mean Fluxes and Seasonal Fluxes in 2021. In 2020, the fluxes were modelled until DOY 254. In 2021, the fluxes in the season after DOY 254 constituted 44.4% of the total seasonal flux, based on the average of the sampling positions. Since the mean in 2020 does not account for the fluxes in the late season, that could explain its lower value in 2021.

The study could be improved by performing calculations for the same periods. The hourly methane flux in the overlapping period from DOY 187 to 254 indicated an increase of 132% from 2020 to 2021, based on the average of the sample positions. According to these data, the different annual means are not only a result of different modelling periods. It rather points toward actual differences between the two years. However, the compared periods are very short and might not be representative.

Furthermore, the temperature has been considered as a reason for the annual differences in methane concentration. The hourly mean temperature between June and September amounted to 6.78 ± 3.26 °C in 2020 and 5.29 ± 2.01 °C in 2021, measured at the weather station in Adventdalen (Norsk Klimaservicesenter, 2022). The water temperature at LP West is closely linked to the air temperature. The hourly mean temperature in the water amounted to 8.43 ± 3.03 °C between June and September of 2020. In 2021, the water temperature amounted to 6.15 ± 2.80 °C during the same period. The diffusion model incorporates the water temperature. An increase in water temperature would lead to a higher flux. However, the model is not very sensitive to temperature, see Figure A1. Despite the decrease in the air and water temperature in 2021, the methane flux showed an increase in 2021. Therefore, annual variabilities in the methane flux are likely not correlated with the temperature changes in this study.

Studies about fluxes could be carried out on longer time scales to get more insights into the significance of these data and the underlying processes.

4.2.2 Methodic Variability

Hypothesis: The methane fluxes differ between the employed methods. The chamber measurements show higher fluxes than the diffusion model, using data from sampling or from an analyzer.

The diffusion model based on the analyzer showed higher fluxes than the chamber measurements, except for position A, processed with exponential regression, see Section 3.3. The lowest results were obtained with the diffusion model based on manual sampling.
The data of the chamber measurements and the data of the diffusion model originate from different positions at the lake, which could complicate the comparison of the results due to spatial variabilities.
The results of the chamber measurements could be lower than the actual flux was, since the set-up of chambers is suspect to the occurrence of leaks. Leaks could have occurred at the intersection between the chamber and the base, or between the base and the surface of the water (Holland et al., 1999).
The placement of the chambers could alter the pressure and temperature inside the chamber (Holland et al., 1999). Due to the chamber, the wind could be eliminated, and wind-driven fluxes underestimated (Wanninkhof and Knox, 1996; Cole and Caraco, 1998; Raymond and Cole, 2001). Moreover, the concentration gradient in methane diminishes immediately upon deployment of the chamber, resulting in an underestimation of the flux (Rolston et al., 1993). Future studies could shorten the time of chamber placement.
While the methane concentration was measured every second in the chamber, the temperature was replaced with a constant value, measured in Adventdalen. This inaccurate replacement could have affected the results of the chamber measurements.
The results for the diffusion model could be higher through the application of another model. Previous studies on a boreal lake computed the seasonal flux with two types of diffusion models (López Bellido et al., 2009). One followed the approach by Cole and Caraco (1998) using the gas transfer velocity k, similarly to the model in this study. The other diffusion model used the approach by Phelps et al. (1998), which replaced k with the product of the temperature-sensitive diffusion coefficient D and the wind-sensitive boundary layer thickness z. The study found considerable differences between the two models. The diffusion model by Phelps et al. showed a seasonal flux that was 11.1% higher than the flux computed with the model by Cole and Caraco for autumn 2004 between DOY 290 and 322, and 2.56% higher for spring in 2005 between DOY 117 and 132. This shows that the applied diffusion model in my study could underestimate the fluxes. Applying the approach by Phelps et al. at LP West could yield higher fluxes. Nevertheless, the results obtained with the diffusion model were lower than the results obtained with chamber measurements in the study of López Bellido et al.. They found that the seasonal flux in autumn 2004 of the chamber measurements was 30% higher than of the diffusion model by Phelps et al.. In spring 2005, the flux of the chamber measurements was 12.5% higher than that of the diffusion model.
Furthermore, the frequency of the methane concentration measurements could affect the seasonal fluxes. In this study, sampling was conducted on 11 days during the seasons. The time in between was interpolated in one-hour steps. The analyzer method tracked the methane concentration in one-hour steps. In the study of López Bellido et al. (2009), they used a daily sampling frequency. They could compare their result to a flux estimation, based on weekly sampling in the same period. The flux based on daily sampling was 1.5 to 2 times higher than the flux based on weekly sampling. Therefore, the seasonal flux calculated based on the analyzer could be higher and more realistic than the flux calculated from interpolated samples.
Another problem with the diffusion model used in this study could be the inaccurate flux estimations at wind speeds below 3.70 $m \cdot s^{-1}$ (Kankaala et al., 2006). 34.0% of the hours (June and September) in 2020 showed mean wind speeds below 3.70 $m \cdot s^{-1}$. In 2021, the same occurred.

During that time, the flux could be underestimated due to the neglected influence of processes such as convective cooling or precipitation (Kankaala et al., 2006; Wanninkhof, 2014).
Methane ebullition was observed at LP West in 2021. However, the diffusion model omits the ebullition flux. In August 2021, I performed measurements with a bubble trap to quantify the amount of gas that is released through ebullition from LP West. These data showed 30.0 ml$\cdot$ min^{-1} of gas release, which would amount to 9.76 gCH_4 $\cdot min^{-1}$, given a plausible methane concentration of 70.0% (Thompson et al., 2016). The chamber measurements would not be suitable to capture the methane flux, as the gas is too concentrated to be measured by a Los Gatos Research greenhouse gas analyzer attached to the chamber.
Future studies could combine the diffusion model and chamber measurements with bubble traps (Burke et al., 2019; Walter et al., 2008; Wik et al., 2013). This would be a potential methodological solution for solving the spatial and temporal issues of measuring total methane release from lakes (Jammet et al., 2017).

4.2.3 Potential Response of the Methane Fluxes to Climate Warming

The methane flux from pingos could increase due to the warming climate in the higher latitudes, and its consequences on the permafrost, groundwater flow, and carbon transport (Hornum et al., 2020; Bense et al., 2012). Warming of the land surface potentially causes the melt of the ice content in permafrost proceeding from the top down. Less ice content could facilitate the water flow from deeper groundwater aquifers to springs at the surface. According to model calculations, the increase in water flow to the surface amounts to 0.5–1% per year in the period 100–200 years after the initiation of warming in the permafrost regions (Bense et al., 2012). As the groundwater might contain dissolved methane, an increase in groundwater flow would lead to more dissolved methane available in springs and surface waters. The higher the content of dissolved methane in lakes, the higher would be the flux to the atmosphere.
However, the increase in groundwater flow due to climate warming could be compensated by the process of permafrost expansion. The expansion of permafrost in Svalbard is known to be associated with isostatic rebound which exposes sediments from the sea floor to colder atmospheric temperatures (Hodson et al., 2020). The downward shift of the freezing front would rather inhibit the movement of water, and hence the methane transport to surface waters and the methane flux to the atmosphere.
Current temperature changes could also trigger the instability and release of methane clathrates in fjord sediments and deep sediments onshore in the region of LP (Rodés i Llorens, 2021; Betlem et al., 2018, 2021). Methane clathrates are stable at low temperatures and high pressure. Rising temperatures might lead to clathrate dissociation and the release of free, dissolved methane. The timescale of the response depends on the effective permeability and the initial distribution of clathrates (Marín-Moreno et al., 2013)
Climate warming could trigger an increase in the production of biogenic methane in the Arctic lakes (Townsend-Small et al., 2017). The methane found in LP West is thought to mainly originate from past biogenic production (Jacobsen, 2020). It is not clear whether there is still biogenic methane production in the sediments that lie beneath the coastal permafrost layer (Hodson et al., 2019). However, the presence of biogenic methane production in the bottom sediments of LP West is unlikely (Jacobsen, 2020). Climate warming would have no significant effect on the methane production, given that nowadays there is no biogenic methane production in the bottom sediments of LP West.

4.2.4 Relevance in the Methane Budget

In 2020, the Seasonal Flux amounted to 1.69 $gCH_4 \cdot 100$ d $\cdot m^{-2}$ for the average of the sample positions at LP West. In 2021, the Seasonal Flux amounted to 8.17 $gCH_4 \cdot 100$ d $\cdot m^{-2}$ for the average of the sample positions.

These results are lower than the ones, measured in 2017 at LP East amounting to 46.0 $gCH_4 \cdot 100$ $d \cdot m^{-2}$. LP has been reported as "emission hotspot" for methane in the summer season (Hodson et al., 2020, 2019). This was based on a comparison between the methane emissions of LP East and the surrounding wetlands. The wetlands were estimated to have a (median) flux of 1.00–2.00 $gCH_4 \cdot 100$ $d \cdot m^{-2}$ (Pirk et al., 2017). The results of my study still support the assumption that LP emits more methane per square meter than the surrounding wetlands in summer.
Taking into account that the summer flux of LP East constituted approximately only one-quarter of the annual flux in 2017 (Hodson et al., 2019), the annual methane emissions could range between 8.19 and 39.6 $gCH_4 \cdot 100$ $d \cdot m^{-2}$ at LP West. This is much higher than estimations for high-latitude lakes and ponds amounting to 0.500–9.20 $gCH_4 \cdot 100$ $d \cdot m^{-2}$ (Bartlett et al., 1992; Whalen and Reeburgh, 1990).

5 Conclusion

For the first time, the methane concentration was monitored at LP West. The monitoring was performed using manual samples and an automatic methane analyzer. The methane flux was calculated based on a diffusion model for the summer season of 2020 and 2021. Additional chamber measurements were applied to measure the methane flux in August 2021.
The methane concentration indicated a high spatial variability between the position near the inflow and the other positions, which were located at the outflow and near the Western margin. The position at the inflow indicated the highest methane concentrations. In 2020, the mean of the inflow position amounted to 1.13 $\pm$ 2.78 mg$\cdot$ l^{-1}. The mean of 2021, amounted to 2.47 $\pm$ 2.72 mg$\cdot$ l^{-1}. The dissolved methane found in LP West could originate from the transport of methane-rich groundwater into the lake.
I could find different seasonal patterns in methane concentration, with low concentrations down to 0 mg$\cdot$ l^{-1} after the melt season. The seasonal variability at LP West could depend on the hydrological, meteorological forcing, and methanotrophic activities.
The data reflected an increase of 383% in the seasonal flux from 2020 to 2021. The annual variability in the methane flux could be linked to annual variabilities in the methane concentration, and the mean seasonal wind speed.
The employed methods resulted in different estimations for the methane flux, whereby the diffusion model, using the data from the automatic analyzer, obtained the highest results. An exception to this was the estimation of the chamber measurements, processed with exponential regression at position A. Future studies should take the ebullition flux into account, which could be measured through bubble traps.
The summer emissions, amounting to 1.69–8.17 $gCH_4 \cdot 100$ d $\cdot m^{-2}$ for the average of the sample positions at LP West, exceeded those of the surrounding wetlands. This reinforced the statement that pingos could be a stronger source of methane emissions than wetlands. Because pingos are a regional methane emission hotspot, they are worth being studied further, especially given the potential response of underlying methane clathrates to climate warming.

Acknowledgement

First of all, I would like to thank Claire, for supervising me in the process of analyzing the data and writing my thesis. I felt always welcome to engage in the PermaFlux Group at the Awi and ask questions. I am also greatly thankful to my supervisor Ulrike, who agreed to become my supervisor only a few minutes after I had sent the request and helped me with all the formalities, that were necessary to go to Svalbard. Thank you Andy for all the instructions and trust to use the equipment and technique, and the supervision after my time on Svalbard. Special thanks also go to my friends Xenia ("Leidensgenossin"), Jonas, and John, who helped me out in the field. I will never forget how we tried to cross a very muddy area on foot and how we looked afterward. I am very thankful to the master's students Tomi and Marjolein for all the work together in the field, and their expertise. Thank you very much Lea for proofreading and advice! I would especially like to thank my family and Mattia, I could not imagine the last months without you, and I am looking forward to what is coming next. Thank you all very much!

References

C. Achtnich, F. Bak, and R. Conrad. Competition for electron donors among nitrate reducers, ferric iron reducers, sulfate reducers, and methanogens in anoxic paddy soil. *Biology and Fertility of Soils*, 19:65–72, 01 1995. doi: 10.1007/BF00336349.

J. Arnfield. Köppen climate classification. *Encyclopedia Britannica*, 2020. `https://www.britannica.com/science/Koppen-climate-classification`, access on 10 July 2022.

K. Bartlett, P. Crill, R. Sass, R. Harriss, and N. Dise. Methane emissions From Tundra environments in the Yukon-Kuskokwim Delta, Alaska. *J. Geophys. Res.*, 97:16645–16660, 11 1992. doi: 10.1029/91JD00610.

L. Bengtsson. Mixing in ice-covered lakes. *Hydrobiologia*, 322:91–97, 04 1996. doi: 10.1007/BF00031811.

V. Bense, H. Kooi, G. Ferguson, and T. Read. Permafrost degradation as a control on hydrogeological regime shifts in a warming climate. *Journal of Geophysical Research (Earth Surface)*, 117, 04 2012. doi: 10.1029/2011JF002143.

P. Betlem, K. Senger, and A. Hodson. 3D thermobaric modelling of the gas hydrate stability zone onshore central Spitsbergen, Arctic Norway. *Marine and Petroleum Geology*, 100:246–262, 11 2018. doi: 10.1016/j.marpetgeo.2018.10.050.

P. Betlem, S. Roy, T. Birchall, A. Hodson, R. Noormets, M. Römer, R. Skogseth, and K. Senger. Modelling of the gas hydrate potential in Svalbard's fjords. *Journal of Natural Gas Science and Engineering*, 94, 07 2021. doi: 10.1016/j.jngse.2021.104127.

D. Bouffard and A. Wuest. Convection in lakes. *Annual Review of Fluid Mechanics*, 51:189–215, 01 2019. doi: 10.1146/annurev-fluid-010518-040506.

S. Burke, M. Wik, A. Lang, A. Contosta, M. Palace, P. Crill, and R. Varner. Long-term measurements of methane ebullition from thaw ponds. *Journal of Geophysical Research: Biogeosciences*, 124:2208–2221, 07 2019. doi: 10.1029/2018JG004786.

D. Capone and R. Kiene. Comparison of microbial dynamics in marine and freshwater sediments: Contrasts in anaerobic carbon catabolism. *Limnology and Oceanography*, 33:725–749, 07 1988. doi: 10.4319/lo.1988.33.4part2.0725.

T. Carleton and S. Hsiang. Social and economic impacts of climate. *Science*, 353:aad9837–1–aad9837–15, 09 2016. doi: 10.1126/science.aad9837.

J. Cole and N. Caraco. Atmospheric exchange of carbon dioxide in a low-wind oligotrophic lake measured by the addition of SF6. *Limnology and Oceanography*, 43:647–656, 06 1998. doi: 10.4319/lo.1998.43.4.0647.

A. Cortés and S. Macintyre. Mixing processes in small arctic lakes during spring. *Limnology and Oceanography*, 65:260–288, 08 2019. doi: 10.1002/lno.11296.

R. Delaune, C. Smith, W. PATRICK, and W. Jr. Methane release from Gulf coast wetlands. *Tellus B*, 35B:8–15, 02 1983. doi: 10.1111/j.1600-0889.1983.tb00002.x.

B. Denfeld, M. Ricão Canelhas, G. Weyhenmeyer, S. Bertilsson, A. Eiler, and D. Bastviken. Constraints on methane oxidation in ice-covered boreal lakes: Constraints on ch_4 oxidation in lakes. *Journal of Geophysical Research: Biogeosciences*, 121:1924–1933, 07 2016. doi: 10.1002/2016JG003382.

W. Eugster, G. Kling, T. Jonas, J. McFadden, A. Wuest, S. Macintyre, and F. S. Chapin III. CO_2 exchange between air and water in an Arctic Alaskan and midlatitude Swiss lake: Importance of convective mixing. *Journal of Geophysical Research Atmospheres*, 108, 06 2003.

D. Farmer. Penetrative convection in the absence of mean shear. *Quart. J. Roy. Meteor. Soc.*, 101:869–891, 10 1975. doi: 10.1002/qj.49710143011.

P. Forster, V. Ramaswamy, P. Artaxo, T. Berntsen, R. Betts, D. Fahey, J. Haywood, J. Lean, D. Lowe, G. Myhre, J. Nganga, R. Prinn, G. Raga, M. Schulz, R. Dorland, G. Bodeker, O. Boucher, W. Collins, T. Conway, and T. Whorf. Changes in atmospheric constituents and in radiative forcing. publicly available on ResearchGate, 10 2007.

H. French. *Periglacial environments*, page 136. Wiley Blackwell, 12 2007. ISBN 978-1-119-13278-3.

S. Greene, K. Walter Anthony, D. Archer, A. Sepulveda-Jauregui, and K. Martinez-Cruz. Modeling the impediment of methane ebullition bubbles by seasonal lake ice. *Biogeosciences*, 11: 6791–6811, 12 2014. doi: 10.5194/bg-11-6791-2014.

C. Hammock, B. Kulessa, J. Hiemstra, A. Hodson, and A. Hubbard. Seismic and electrical geophysical characterization of an incipient coastal open-system pingo: Lagoon pingo, svalbard. *Earth and Space Science*, 9, 03 2022. doi: 10.1029/2021EA002093.

I. Hanssen-Bauer, E. J. Førland, H. Hisdal, S. Mayer, A. B. Sandø, and A. Sorteberg. Climate in Svalbard 2100 – a knowledge base for climate adaptation, 01 2019. `https://www.miljodirektoratet.no/globalassets/publikasjoner/M1242/M1242.pdf"`, access on 10 July 2022.

A. Heginbottom, J. Brown, O. Humlum, and H. Svensson. State of the Earth's cryosphere at the beginning of the 21st century: Glaciers, global snow cover, floating ice, and permafrost and periglacial environments - permafrost and periglacial environments. *USGS Professional Paper 1386*, pages 795–796, 2012. doi: 10.3133/pp1386A.

A. Hodson, A. Nowak, E. Mannerfelt, K. Redeker, A. Turchyn, and H. Christiansen. Seasonal dynamics of methane and carbon dioxide evasion from an open system pingo: Lagoon Pingo, Svalbard. *Frontiers in Earth Science*, 7, 02 2019. doi: 10.3389/feart.2019.00030.

A. Hodson, A. Nowak, M. Hornum, K. Senger, K. Redeker, H. Christiansen, S. Jessen, P. Betlem, S. Thornton, A. Turchyn, S. Olaussen, and A. Marca. Sub-permafrost methane seepage from open-system pingos in Svalbard. *The Cryosphere*, 14:3829–3842, 11 2020. doi: 10.5194/tc-14-3829-2020.

E. Holland, G. P. Robertson, J. Greenberg, P. Groffman, R. Boone, and J. Gosz. Soil CO_2, N_2O, and CH_4 exchange. *Standard Soil Methods for Long-Term Ecological Research*, pages 185–201, 01 1999.

M. Hornum. Postglacial rebound, permafrost growth, and its impact on groundwater flow and pingo formation - An investigation combining electrical resistivity tomography, hydrogeochemistry and decoupled heat and groundwater transport modelling, Adventdalen, Svalbard. Master's thesis, University of Copenhagen, 06 2018.

M. Hornum, A. Hodson, S. Jessen, V. Bense, and K. Senger. Numerical modelling of permafrost spring discharge and open-system pingo formation induced by basal permafrost aggradation. *The Cryosphere*, 14:4627–4651, 12 2020. doi: 10.5194/tc-14-4627-2020.

T. J. Jacobsen. Modelling of Methanogenesis in a Subpermafrost Environment resulting in D-excess in Pingo Spring Water in Adventdalen, Svalbard. Bachelor's Thesis, University of Copenhagen, 08 2020.

M. Jammet, P. Crill, S. Dengel, and T. Friborg. Large methane emissions from a subarctic lake during spring thaw: Mechanisms and landscape significance. *Journal of Geophysical Research: Biogeosciences*, 120:2289–2305, 11 2015. doi: 10.1002/2015JG003137.

M. Jammet, S. Dengel, E. Kettner, F.-J. Parmentier, M. Wik, P. Crill, and T. Friborg. Year-round CH_4 and CO_2 flux dynamics in two contrasting freshwater ecosystems of the subarctic. *Biogeosciences Discussions*, pages 1–49, 01 2017. doi: 10.5194/bg-2016-466.

J. Jansen, B. Thornton, A. Cortés, J. Snöälv, M. Wik, S. Macintyre, and P. Crill. Drivers of diffusive CH_4 emissions from shallow subarctic lakes on daily to multi-year timescales. *Biogeosciences*, 17:1911–1932, 04 2020. doi: 10.5194/bg-17-1911-2020.

H. Jiang, Y. Chen, P.-X. Jiang, C. Zhang, T. Smith, J. Murrell, and X.-H. Xing. Methanotrophs: Multifunctional bacteria with promising applications in environmental bioengineering. *Biochemical Engineering Journal*, 49:277–288, 05 2010. doi: 10.1016/j.bej.2010.01.003.

E. L. Jones. *The biogeochemistry of the active layer and shallow permafrost in a High Arctic fjord valley, Svalbard*. PhD thesis, University of Sheffield, 09 2019.

A. Joseph. *Secrets of Bermuda Triangle and Formation of Polymetallic Nodules*, pages 81–138. Elsevier, 01 2017. ISBN 9780128093573. doi: 10.1016/B978-0-12-809357-3.00002-3.

P. Kankaala, J. Huotari, E. Peltomaa, T. Saloranta, and A. Ojala. Methanotrophic activity in relation to methane efflux and total heterotrophic bacterial production in a stratified, humic, boreal lake. *Limnology and oceanography*, 51:1195–1204, 03 2006. doi: 10.4319/lo.2006.51.2.1195.

G. Kirillin, M. Leppäranta, A. Terzhevik, N. Granin, J. Krüger, C. Engelhardt, T. Efremova, S. Golosov, N. Palshin, P. Sherstyankin, G. Zdorovennova, and R. Zdorovennov. Physics of seasonally ice-covered lakes: A review. *Aquatic Sciences*, 74:659–682, 10 2012. doi: 10.1007/s00027-012-0279-y.

G. Kirillin, I. Aslamov, M. Leppäranta, and E. Lindgren. Turbulent mixing and heat fluxes under lake ice: the role of seiche oscillations. *Hydrology and Earth System Sciences Discussions*, page 6493–6504, 07 2018. doi: 10.5194/hess-2018-376.

G. Kraev, E. Rivkina, T. Vishnivetskaya, A. Belonosov, K. Van Huissteden, A. Kholodov, A. Smirnov, A. Kudryavtsev, K. Teshebaeva, and Z. Dmitry. Methane in gas shows from boreholes in epigenetic permafrost of Siberian Arctic. *Geosciences (Switzerland)*, 9, 01 2019. doi: 10.3390/geosciences9020067.

A. Lecher, N. Dimova, K. Sparrow, F. Garcia-Tigreros, J. Murray, S. Tulaczyk, and J. Kessler. Methane transport from the active layer to lakes in the Arctic using Toolik Lake, Alaska, as a case study. *Proceedings of the National Academy of Sciences of the United States of America*, 112:3636–3640, 03 2015. doi: 10.1073/pnas.1417392112.

A. Lecher, P.-C. Chuang, and M. Singleton. Sources of methane to an Arctic lake in Alaska: An isotopic investigation: Arctic lake methane and water isotopes. *Journal of Geophysical Research: Biogeosciences*, 122:753–766, 03 2017. doi: 10.1002/2016JG003491.

O. Liestøl. Pingos, springs and permafrost in spitsbergen. *Norsk Polarinst. Årbok*, 1975:7–29, 01 1977.

P. Liss and P. Slater. Flux of gases across the air-sea interface. *Nature*, 247:181–184, 01 1974. doi: 10.1038/247181a0.

L. Loken, J. Crawford, P. Schramm, P. Stadler, A. Desai, and E. Stanley. Large spatial and temporal variability of carbon dioxide and methane in a eutrophic lake. *Journal of Geophysical Research: Biogeosciences*, 124:2248–2266, 07 2019. doi: 10.1029/2019JG005186.

J. López Bellido, T. Tulonen, P. Kankaala, and A. Ojala. CO_2 and CH_4 fluxes during spring and autumn mixing periods in a boreal lake (Pääjärvi, southern Finland). *Journal of Geophysical Research*, 114, 11 2009. doi: 10.1029/2009JG000923.

I. Lønne and W. Nemec. High-Arctic fan delta recording deglaciation and environment disequilibrium. *Sedimentology*, 51:553 – 589, 06 2004. doi: 10.1111/j.1365-3091.2004.00636.x.

J. Mackay. Pingos of the Tuktoyaktuk Peninsula Area, Northwest Territories. *Géographie physique et Quaternaire*, 33:3–61, 01 1979. doi: 10.7202/1000322ar.

J. Mackay. Pingo growth and collapse, Tuktoyaktuk Peninsula Area, western Arctic coast, Canada: a long-term field study. *Géographie physique et Quaternaire*, 52:271–323, 01 1998. doi: 10.7202/004847ar.

H. Marín-Moreno, T. Minshull, G. Westbrook, B. Sinha, and S. Sarkar. The response of methane hydrate beneath the seabed offshore Svalbard to ocean warming during the next three centuries. *Geophysical Research Letters*, 40:5159–5163, 10 2013. doi: 10.1002/grl.50985.

Microsoft Excel, 2018. Retrieved from `https://office.microsoft.com/excel`.

D. Mironov, A. Terzhevik, G. Kirillin, T. Jonas, J. Malm, and D. Farmer. Radiatively-driven convection in ice-covered lakes: Observations, scaling and mixed-layer model. *J. Geophys. Res.*, 107:1–16, 04 2002. doi: 10.1029/2001JC000892.

F. Müller. Beobachtungen über Pingos. *Meddelelser om Gronland*, 154:127, 01 1959.

F.-J. Nat and J. Middelburg. Effects of two common macrophytes on methane dynamics in freshwater sediments. *Biogeochemistry*, 43:79–104, 10 1998. doi: 10.1023/A:1006076527187.

NILU. Norwegian Institute for Air Research - Database for atmospheric measurement data, 2022. `https://ebas-data.nilu.no/`, access on 10 July 2022.

Norsk Klimaservicesenter. Database for climate data, 2022. `https://seklima.met.no/`, access on 10 July 2022.

NPI. Norwegian Polar Institute - S100 Topographic Raster Data for Svalbard, 1990. `https://doi.org/10.21334/npolar.1990.44ca8c2a`, access on 10 July 2022.

NPI. Norwegian Polar Institute - NP Ortophoto Svalbard WMTS, 2022a. `https://geodata.npolar.no/arcgis/rest/services/Basisdata/NP_Ortofoto_Svalbard_WMTS_25833/MapServer?f=jsapi`, access on 10 July 2022.

NPI. Norwegian Polar Institute - Aerial map of Svalbard, 2022b. `https://toposvalbard.npolar.no/`, access on 10 July 2022.

NSIDC. National Snow and Ice Data Centre - Definition Isostatic Rebound, 2022. `https://nsidc.org/`, access on 10 July 2022.

O. Peltola, M. Raivonen, X. Li, and T. Vesala. Technical note: Comparison of methane ebullition modelling approaches used in terrestrial wetland models. *Biogeosciences Discussions*, 15:1–19, 07 2017. doi: 10.5194/bg-15-937-2018.

A. Phelps, K. Peterson, and M. Jeffries. Methane efflux from high-latitude lakes during spring ice melt. *Journal of Geophysical Research*, 103:29029–29036, 11 1998. doi: 10.1029/98JD00044.

N. Pirk, M. Mastepanov, E. López-Blanco, L. Christensen, H. Christiansen, B. Hansen, M. Lund, F.-J. Parmentier, K. Skov, and T. R. Christensen. Toward a statistical description of methane emissions from Arctic wetlands. *Ambio*, 46:70–80, 02 2017. doi: 10.1007/s13280-016-0893-3.

A. Porsild. Earth mounds in unglaciated Arctic northwestern America. *Geographical Review*, 28:46–58, 01 1938. doi: 10.2307/210565.

QGis, 2018. Free and Open Source Geographic Information System, version 3.10.6.

P. Raymond and J. Cole. Gas exchange in rivers and estuaries: Choosing a gas transfer velocity. *Estuaries and Coasts*, 24:312–317, 04 2001. doi: 10.2307/1352954.

M. Ricão Canelhas, B. Denfeld, G. Weyhenmeyer, D. Bastviken, and S. Bertilsson. Methane oxidation at the water-ice interface of an ice-covered lake. *Limnology and Oceanography*, 61: S78–S90, 03 2016. doi: 10.1002/lno.10288.

J. Riera, J. Schindler, and T. Kratz. Seasonal dynamics of carbon dioxide and methane in two clear-water lakes and two bog lakes in northern Wisconsin, U.S.A. *Canadian Journal of Fisheries and Aquatic Sciences*, 56:265–274, 04 2011. doi: 10.1139/f98-182.

N. Rodés i Llorens. Gas hydrate stability and distribution in the fjords of Western Spitsbergen, Svalbard archipelego. Master's thesis, Hamburg University, Saint Petersburg State University, 09 2021. unpublished work.

D. Rolston, J. Duxbury, L. Harper, A. Mosier, G. Hutchinson, and G. Livingston. *Use of Chamber Systems to Measure Trace Gas Fluxes*. Agricultural Ecosystem Effects on Trace Gases and Global Climate Change, 01 1993. ISBN 9780891181132. doi: 10.2134/asaspecpub55.c4.

RStudio, 2022. R: A Language and Environment for Statistical Computing. R Foundation for Statistical Computing, Vienna, Austria, version: 2022.02.3.

A. Sepulveda-Jauregui, K. Walter Anthony, K. Martinez-Cruz, S. Greene, and F. Thalasso. Methane and carbon dioxide emissions from 40 lakes along a north–south latitudinal transect in Alaska. *Biogeosciences*, 12:3197–3223, 06 2015. doi: 10.5194/bg-12-3197-2015.

E. D. Sloan and C. Koh. *Clathrate hydrates of natural gases, third edition*. Clathrate Hydrates of Natural Gases, Third Edition, 01 2007. ISBN 9780849390784.

D. Stolper, A. Martini, M. Clog, P. Douglas, S. Shusta, D. Valentine, A. Sessions, and J. Eiler. Distinguishing and understanding thermogenic and biogenic sources of methane using multiply substituted isotopologues. *Geochimica et Cosmochimica Acta*, 161:219–247, 07 2015. doi: 10.1016/j.gca.2015.04.015.

R. Striegl, P. Kortelainen, J. Chanton, K. Wickland, G. Bugna, and M. Rantakari. Carbon dioxide partial pressure and 13C content of north temperate and boreal lakes at spring ice melt. *Limnology and Oceanography*, 46:941–945, 06 2001. doi: 10.4319/lo.2001.46.4.0941.

C. Sweeney, M. Gloor, A. Jacobson, R. Key, G. Mckinley, J. Sarmiento, and R. Wanninkhof. Constraining global air-sea gas exchange for CO_2 with recent Bomb 14C measurements. *Global Biogeochemical Cycles*, 21, 06 2007. doi: 10.1029/2006GB002784.

A. Szczucińska. Occurrence and temporal variations of groundwater outflows in the Petuni-abukta region, Spitsbergen. *Polish Polar Research*, 32:361–374, 01 2011. doi: 10.2478/v10183-011-0023-7.

H. Thompson, J. White, L. Pratt, and P. Sauer. Spatial variation in flux, δ13C and δ2H of methane in a small Arctic lake with fringing wetland in western Greenland. *Biogeochemistry*, 131:17–33, 12 2016. doi: 10.1007/s10533-016-0261-1.

A. Townsend-Small, F. Akerstrom, C. Arp, and K. Hinkel. Spatial and temporal variation in methane concentrations, fluxes, and sources in lakes in arctic alaska: Methane in arctic alaskan lakes. *Journal of Geophysical Research: Biogeosciences*, 122, 10 2017. doi: 10.1002/2017JG004002.

K. Walter, J. Chanton, F. S. Chapin III, E. Schuur, S. Zimov, and C. Walter. Methane production and bubble emissions from arctic lakes: Isotopic implications for source pathways and ages. *J. Geophys. Res.*, 113, 09 2008. doi: 10.1029/2007JG000569.

K. Walter Anthony, P. Anthony, G. Grosse, and J. Chanton. Geologic methane seeps along boundaries of Arctic permafrost thaw and melting glaciers. *Nature Geoscience*, 5:419–426, 05 2012. doi: 10.1038/ngeo1480.

R. Wanninkhof. Relationship between wind speed and gas exchange over the ocean revisited. *Limnology and Oceanography*, 12:315–362, 05 2014. doi: 10.1029/92JC00188.

R. Wanninkhof and M. Knox. Chemical enhancement of CO_2 exchange in natural waters. *Limnology and Oceanography*, 41:689–697, 06 1996. doi: 10.4319/lo.1996.41.4.0689.

D. Weisenburg and N. Guinasso. Equilibrium solubilities of methane, carbon monoxide and hydrogen in water and seawater. *J. Chem. Eng. Data*, 24:354–360, 01 1979. doi: 10.1021/je60083a006.

C. Werner, K. Davis, P. Bakwin, C. Yi, D. Hurst, and L. Lock. Regional-scale measurements of CH_4 exchange from a tall tower over a mixed temperate/boreal lowland and wetland forest. *Global Change Biology*, 9:1251 – 1261, 08 2003. doi: 10.1046/j.1365-2486.2003.00670.x.

S. Whalen and W. Reeburgh. A methane flux transect along the Trans-Alaska-Pipeline Haul Road. *Tellus B*, 42:237–249, 08 1990. doi: 10.1034/j.1600-0889.1990.t01-2-00002.x.

M. Wik, P. Crill, R. Varner, and D. Bastviken. Multiyear measurements of ebullitive methane flux from three subarctic lakes. *Journal of Geophysical Research: Biogeosciences*, 118:1307–1321, 09 2013. doi: 10.1002/jgrg.20103.

P. Worsley and S. Gurney. Geomorphology and hydrogeological significance of the Holocene pingos in the Karup Valley area, Traill Island, northern east Greenland. *Journal of Quaternary Science - J QUATERNARY SCI*, 11:249–262, 05 1996. doi: 10.1002/(SICI)1099-1417(199605/06)11:33.0.CO;2-4.

www.salinometry.com. Practical salinity calculator, 2022. `https://salinometry.com/ctd-salinity-calculator`, access on 10 July 2022.

S. Yamamoto, J. Alcauskas, and T. Crozier. Solubility of methane in distilled water and seawater. *Journal of Chemical and Engineering Data*, 21:78–80, 01 1976. doi: 10.1021/je60068a029.

K. Yoshikawa and K. Harada. Observations on nearshore pingo growth, Adventdalen, Spitsbergen. *Permafrost and Periglacial Processes*, 6:361 – 372, 10 1995. doi: 10.1002/ppp.3430060407.

Appendix

DOY 2020	**Position Infow**	**Position Outflow**
176	16.623	0.000
184	1.333	0.011
194	0.064	0.000
201	0.091	-
207	0.094	-
219	0.187	0.0602
230	0.092	0.002
244	0.129	0.332
254	0.266	0.542
260	1.134	1.201
267	2.436	1.583

Table A1: Methane concentration of the samples from the position at the inflow and outflow in $mg \cdot l^{-1}$ for the year 2020.

DOY 2021	**Position Inflow**	**Position Outflow**	**Position Margin**	**Position Central North**
187	-	0.000402	0.00	0.000499
196	0.38856	0.462276	0.001171	0.032066
208	0.027817	0.028454	0.00187	-
219	0.114222	0.001975	0.002303	-
222	0.067029	0.043903	0.002286	-
226	0.00099	0.003763	0.005558	-
229	1.562325	0.012547	0.190984	-
240	8.509059 5.183392	0.658099 0.683193	0.826867 0.72793	-
254	5.084184 5.056751	5.298524 5.025512	5.221628	-
270	1.044153	0.06539 1.192078	0.63458 0.014833 1.027085	-
274	2.869368	2.13861 2.21411	-	-

Table A2: Methane concentration of the samples from the position at the inflow, outflow, margin, and central North in $mg \cdot l^{-1}$ for the year 2021.

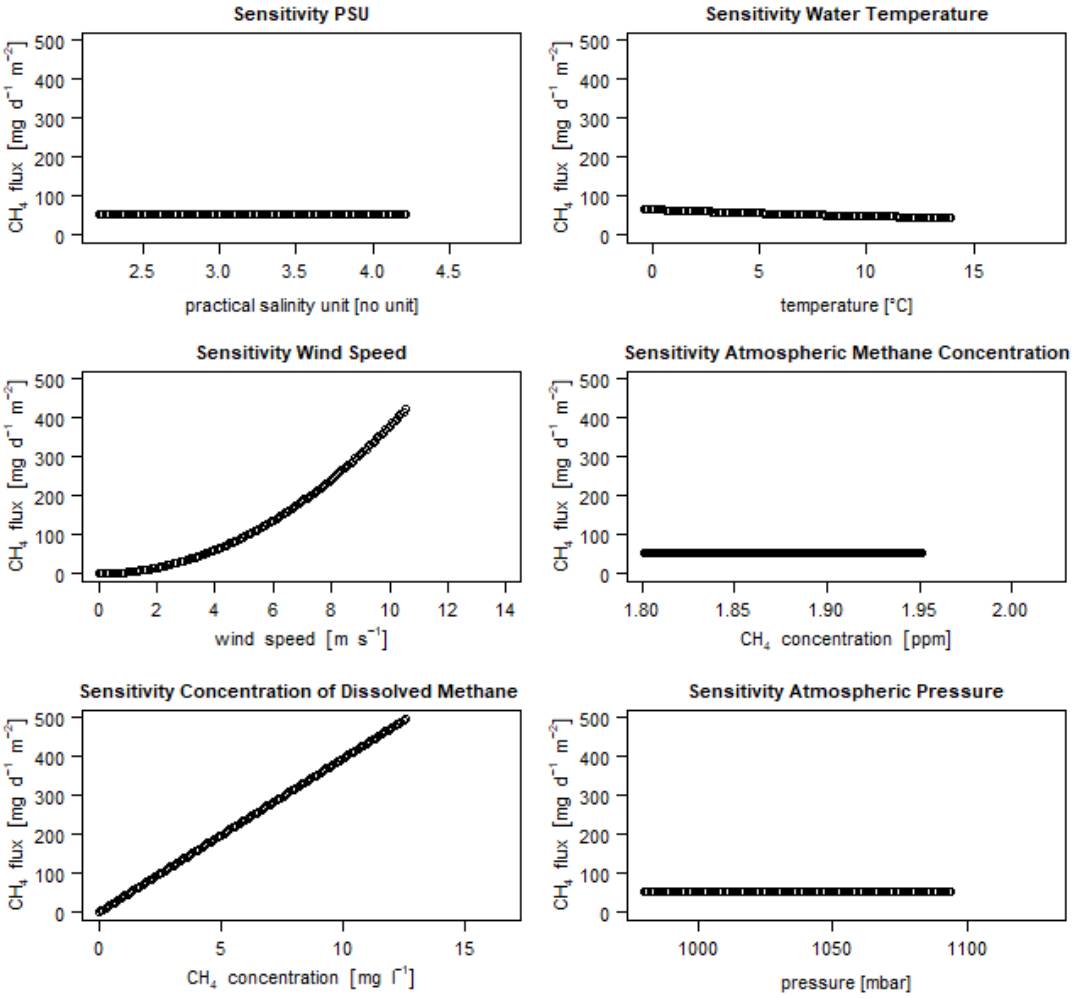

Figure A1: Sensitivity of methane flux to the variables salinity (PSU), wind speed, dissolved methane concentration, water temperature, atmospheric methane concentration, and atmospheric pressure, for more information of the methods see section 2.3.2, the model is most sensitive to the variables wind speed and concentration of dissolved methane.

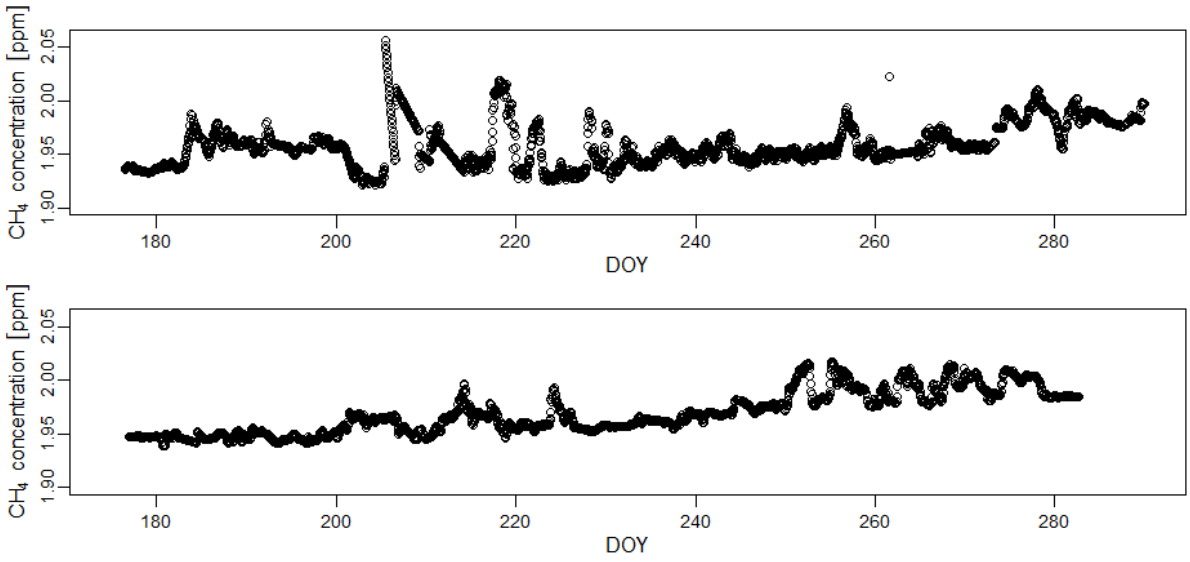

Figure A1: Top: Methane concentration in the atmosphere in ppm on Svalbard, Ny Alesund over summer season in 2020. Bottom: Equivalent data as in the upper plot but for 2021.

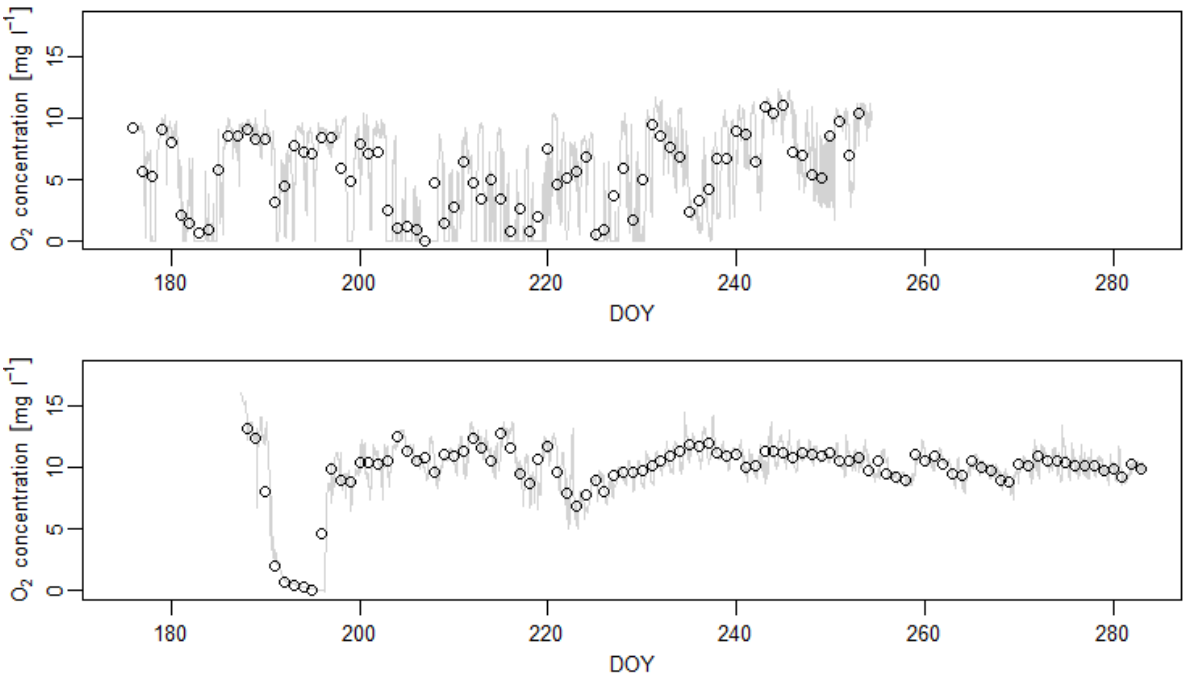

Figure A2: Top: Oxygen concentration in the water of LP West in $mg \cdot l^{-1}$ measured through a Campbell logger in 2020. Bottom: Equivalent data as in the upper plot but for 2021. Points are the daily means and the grey line is the interpolated record in one-hour steps.

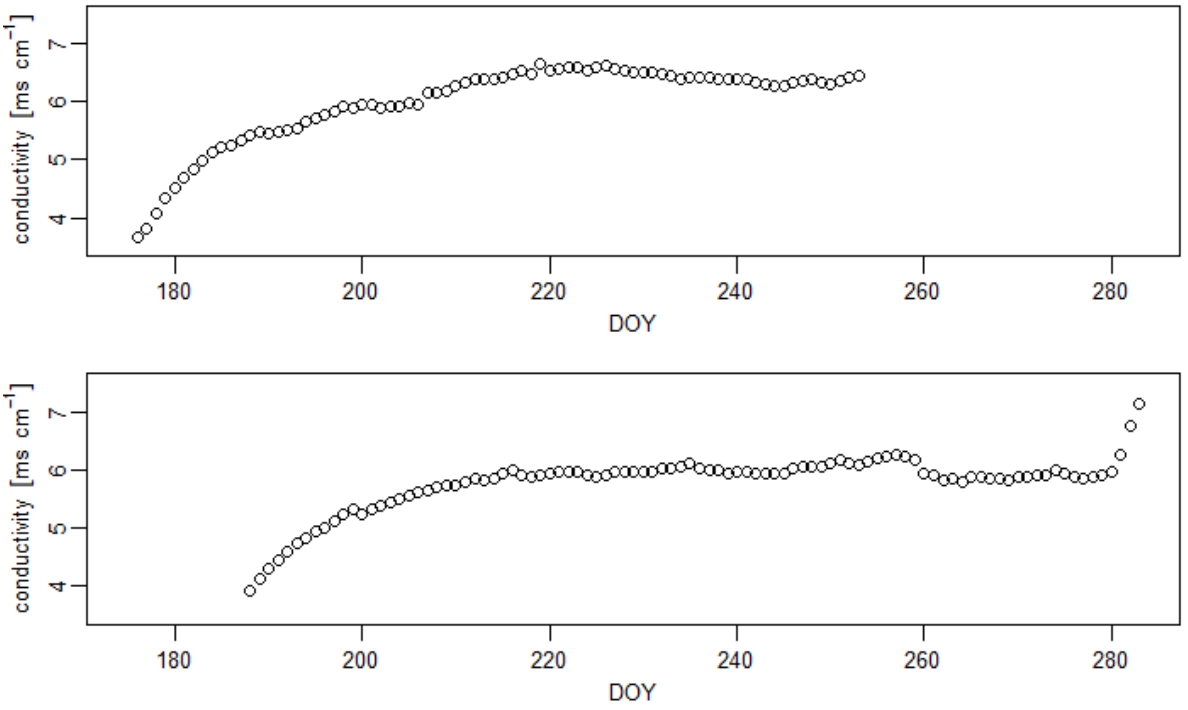

Figure A3: Top: Daily mean electrical conductivity in $mS \cdot cm^{-1}$ in the water of LP West measured through a Campbell logger in 2020. Bottom: Equivalent data as in the upper plot but for 2021.

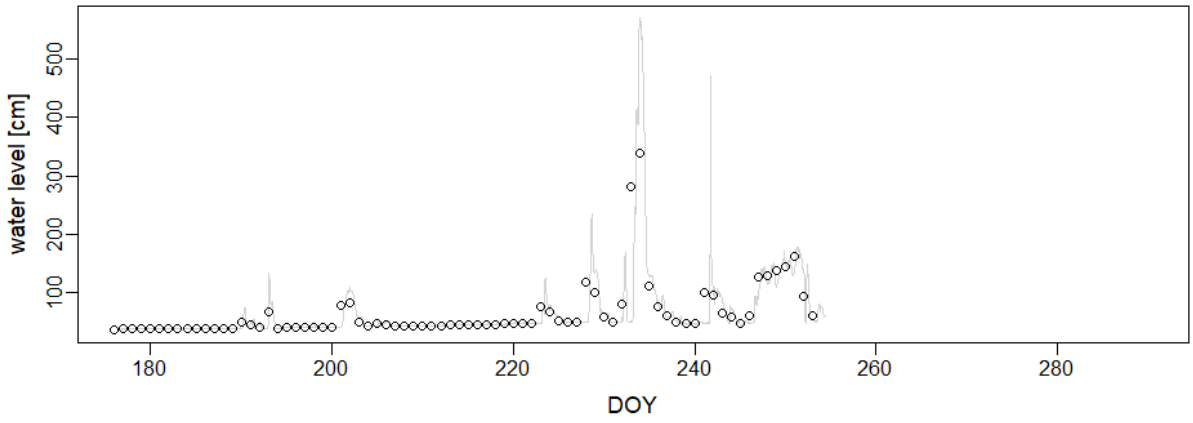

Figure A4: Water level at LP West in cm measured through a Campbell logger in 2020, point are the daily means of the water level.

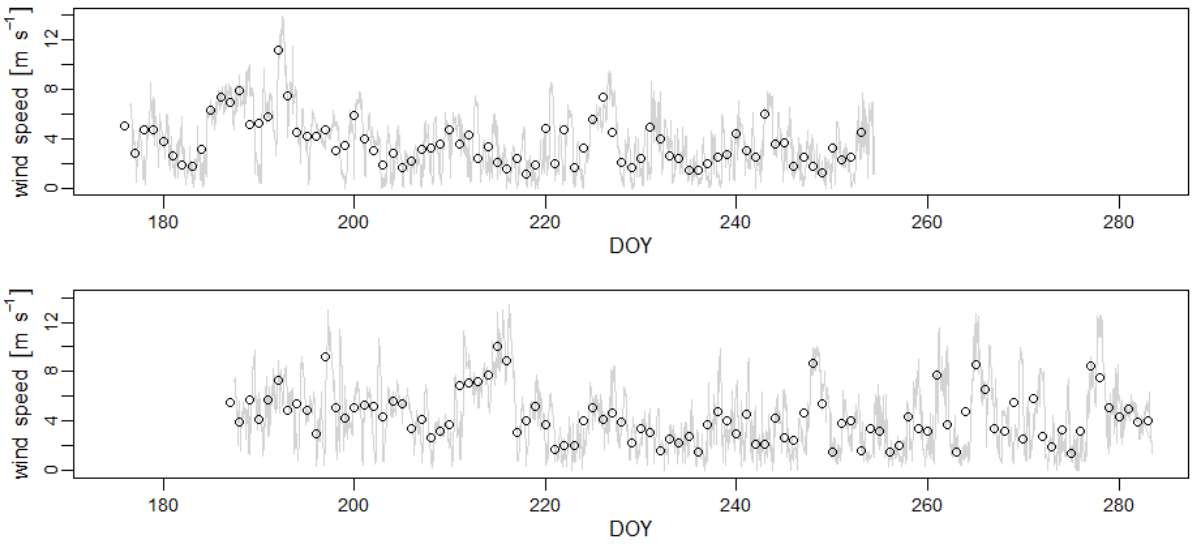

Figure A5: Top: Wind speed in $m \cdot s^{-1}$ at Adventdalen weather station in 2020. Bottom: Equivalent data as in the upper plot but for 2021. Points are the daily means and the grey line is the interpolated record in one-hour steps.

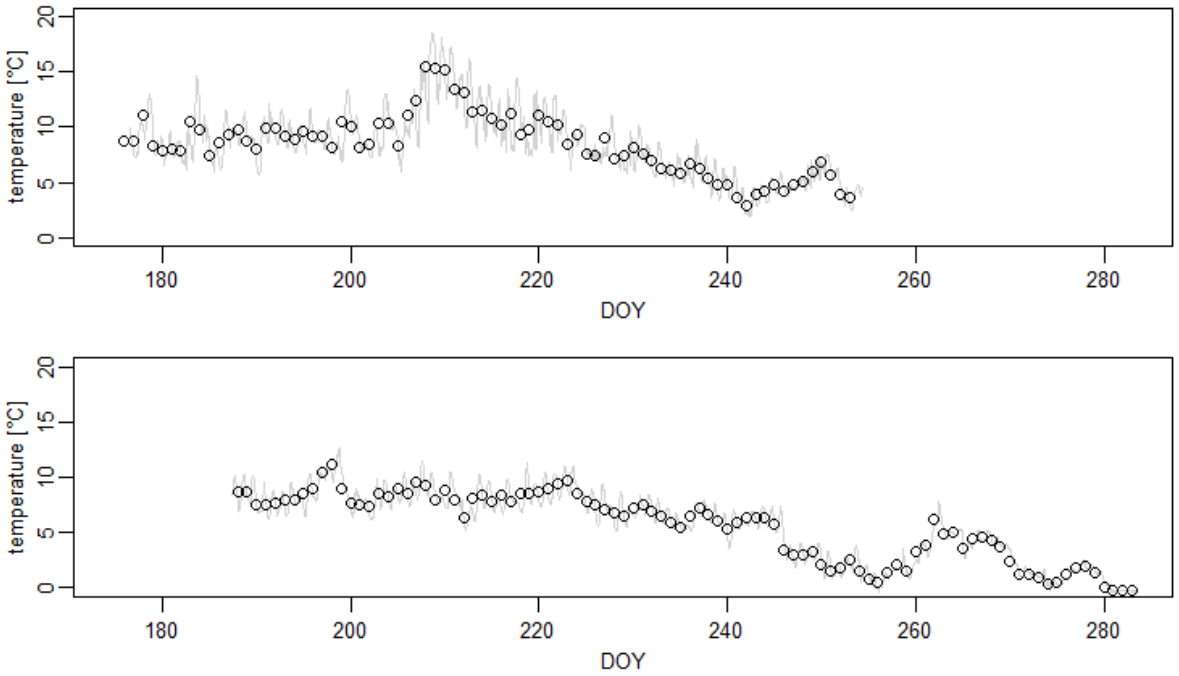

Figure A6: Top: Lake temperature in $^{\circ}C$ in LP West in 2020. Bottom: Equivalent data as in the upper plot but for 2021. Points are the daily means and the grey line is the interpolated record in one-hour steps.

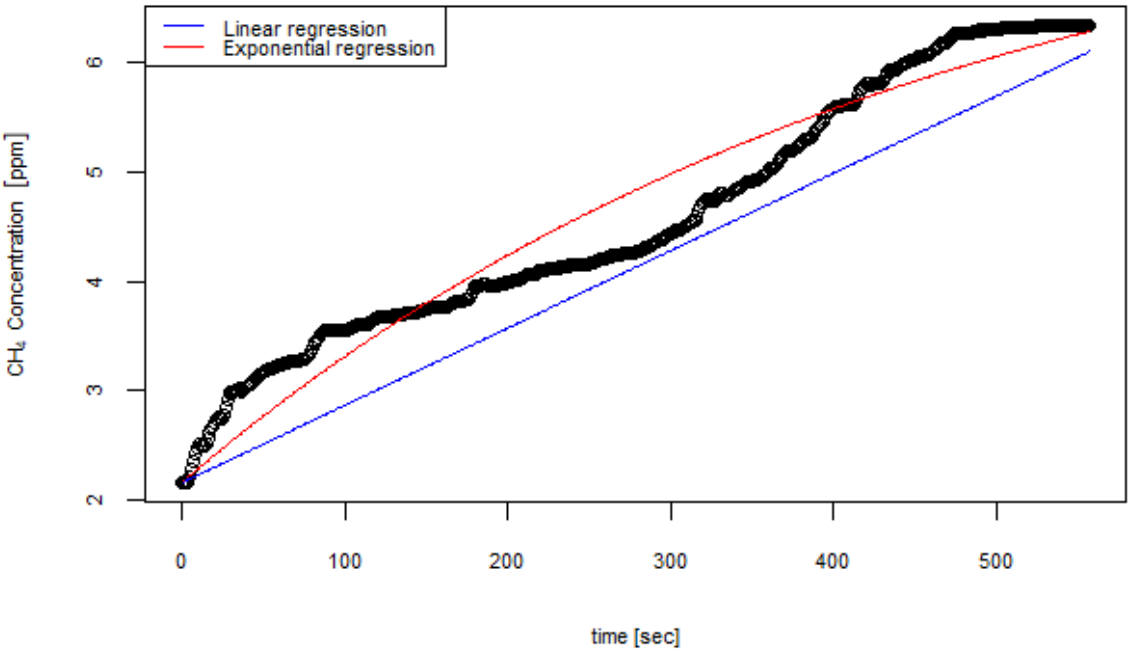

Figure A7: Methane concentration in ppm in chamber of approximately 70 l volume over a period of 557 sec at position A in 2021.

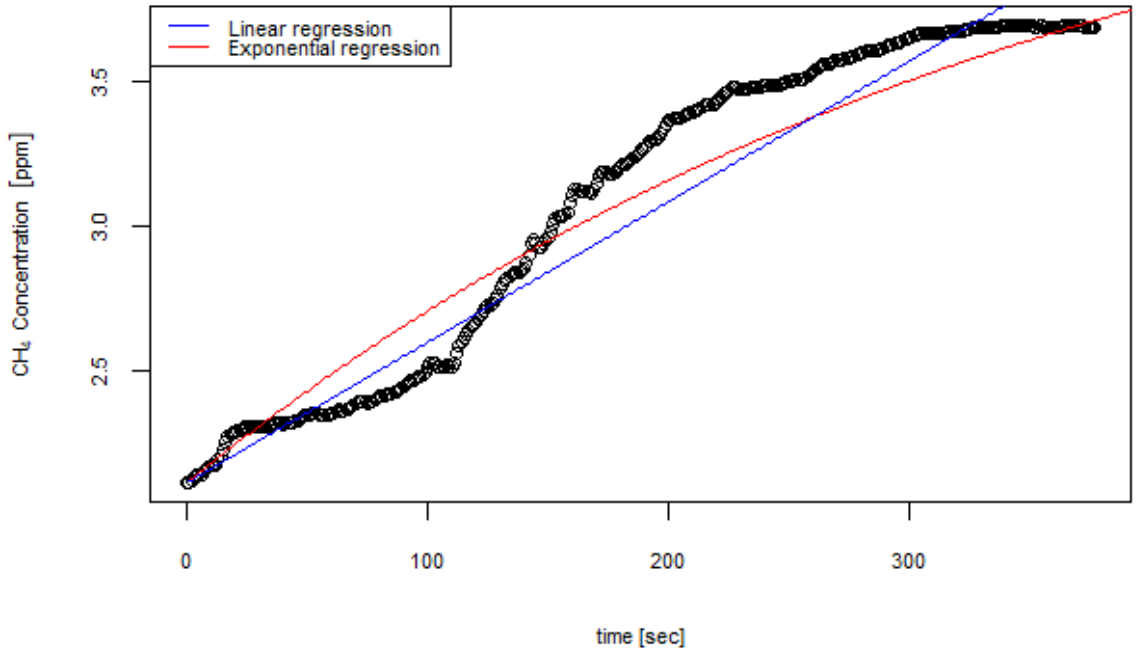

Figure A8: Methane concentration in ppm in a closed chamber of approximately 70 l volume over a period of 377 sec at position B in 2021.

R Script

```
#Analyzing the methane concentration of the samples
#2020
dev.off()
par(mfrow=c(1,2), mar = c(2.5, 2.6, 1, 0.2), mgp=c(1.2, 0.5, 0), las=0)
plot(PointPlot2020$doy, PointPlot2020$lwl5, lwd=1, cex.axis=0.7, cex.lab
    =0.8, ylim=c(0,18), col="grey", xlab="DOY", type="b", lty=2, ylab=
    parse(text = "CH[4]~~concentration ~~ group('[', mg * ~~ l^-1, ']')")
    )
lines(PointPlot2020$doy, PointPlot2020$lwl6, lwd=1, col="darkgreen",
    type="b", lty=2)
legend("topright", c("Position Inflow","Position Outflow"), lwd=c(1,1),
    pch=c(1,1), lty=c(2,2), cex=0.7, col = c("grey", "darkgreen"))
#2021
plot(PointPlot2021$doy, PointPlot2021$lwl2, cex.axis=0.7, cex.lab=0.8,
    lwd=1,  ylim=c(0,18), col="green", xlab="DOY", type="b", lty=2, ylab=
    parse(text = "CH[4]~~concentration ~~ group('[', mg * ~~ l^-1, ']')")
    )
lines(PointPlot2021$doy, PointPlot2021$lwl1, lwd=1, col="purple", type="
    b", lty=2)
lines(PointPlot2021$doy, PointPlot2021$lwl3, lwd=1, col="blue", type="b"
    , lty=2)
legend("topright", c("Position Inflow","Position Outflow", "Margin"),
    cex=0.7, pch=c(1,1,1), lwd=c(1,1,1), lty=c(2,2,2), col = c("green", "
    purple", "blue"))
```

```
#Analysing the methane concentration of the analyzer
dev.off()
par(mfrow=c(1,2), mar = c(2.5, 2.6, 1, 0.2), mgp=c(1.2, 0.5, 0), las=0)
plot(Model_2020_Helene$‘Day dec‘, Model_2020_Helene$CH4_a, ylim=c(0,11),
    type = "l", lty=2, cex.axis=0.7, cex.lab=0.8, col="red",xlim=c
   (176.541666666667, 283.5416667),
     xlab="DOY", ylab=parse(text = "CH[4]~~concentration ~~ group(’[’,
        mg * ~~ l^-1, ’]’)"))
lines(Model_2020_Helene$‘Day dec‘, Model_2020_Helene$CH4_aq_mgl, col="
   red",type = "p")
legend(x = "topleft",legend=c("Analyzer 2020", "Interpolation"),
       col=c("red", "red"), pch = c(19, NA), lty = c(NA,2), cex=0.7)
plot(Model_2021_Helene$‘DOY dec‘, Model_2021_Helene$CH4\_a, ylim=c(0,11)
   , type = "p", cex.lab=0.8, cex.axis=0.7, col="orange",xlim=c
   (176.541666666667, 283.5416667),
     xlab="DOY", ylab=parse(text = "CH[4]~~concentration ~~ group(’[’,
        mg * ~~ l^-1, ’]’)"))
legend(x = "topleft",legend=c("Analyzer 2021"),
       col=c("orange"), pch = c(19), cex=0.7)


#Analyzing the atmospheric methane concentration
dev.off()
par(mfrow=c(2,1), mar = c(2.6, 2.6, 1, 1), mgp=c(1.5, 0.5, 0), las=0)
plot(Pingo2020$‘Day dec‘, Pingo2020$pCH4_pct, ylim=c(1.9,2.06), type = "
   p", lty =0.1, xlim=c(175, 290), xlab="DOY", ylab=parse(text = "CH[4]~
   ~concentration ~~ group(’[’,ppm, ’]’)"), cex.lab=0.8, cex.axis=0.8,
   cex.lab=0.7)
plot(Pingo2021$‘DOY dec‘, Pingo2021$pCH4, ylim=c(1.9,2.06),type = "p",
   xlim=c(175, 290), lty =0.1, xlab="DOY", ylab=parse(text = "CH[4]~~
   concentration ~~ group(’[’, ppm, ’]’)"),cex.axis=0.8, cex.lab=0.8,
   main.cex=0.7)


#Analyzing the concentration of dissolved oxygen
SumO22020= tapply(Pingo2020$‘DO (mg/L)‘, Pingo2020$Day, mean)
DataSumO22020 = data.frame(’Day’= row.names(SumO22020), ’O2Day’=
   SumO22020)
SumO22021= tapply(Pingo2021$‘DO mg/L‘, Pingo2021$DOY, mean)
DataSumO22021 = data.frame(’Day’= row.names(SumO22021), ’O2Day’=
   SumO22021)
par(mfrow=c(2,1), mar = c(2.6, 2.6, 1, 1), mgp=c(1.5, 0.5, 0), las=0)
plot(Pingo2020$‘DO (mg/L)‘~Pingo2020$‘Day dec‘, ylim=c(0,18), type = "l"
   , lty = 1, col="lightgrey", xlim=c(175, 283),cex.axis=0.8, cex.lab
   =0.8, xlab="DOY", ylab=parse(text = "O[2]~~concentration ~~ group
   (’[’, mg * ~~ l^-1, ’]’)"))
points(DataSumO22020$O2Day~DataSumO22020$Day)
plot(Pingo2021$‘DO mg/L‘~Pingo2021$‘DOY dec‘, ylim=c(0,18), type = "l",
   lty = 1, col="lightgrey", xlim=c(175, 283), cex.axis=0.8, cex.lab
   =0.8,xlab="DOY", ylab=parse(text = "O[2]~~concentration ~~ group(’[’,
    mg * ~~ l^-1, ’]’)"))
points(DataSumO22021$O2Day~DataSumO22021$Day)



#Analyzing the wind speed
SumWind2020= tapply(Pingo2020$‘Wind vel (m/s)‘, Pingo2020$Day, mean)
DataSumWind2020 = data.frame(’Day’= row.names(SumWind2020), ’WDay’=
```

```
   SumWind2020)
SumWind2021= tapply(Model_2021n$`Wind vel (m/s)`, Model_2021n$DOY, mean)
DataSumWind2021 = data.frame('Day'= row.names(SumWind2021), 'WDay'=
   SumWind2021)
dev.off()
par(mfrow=c(2,1), mar = c(2.6, 2.6, 1, 1), mgp=c(1.5, 0.5, 0), las=0)
plot(Pingo2020$`Wind vel (m/s)`~Pingo2020$`Day dec`, ylim=c(0,14), col="
   lightgrey",xlim=c(175, 283),cex.axis=0.8, cex.lab=0.8, type = "l",
   lty = 1, xlab="DOY", ylab=parse(text = "wind ~~ speed~~ group('[', m
   * ~~ s^-1, ']')"))
points(DataSumWind2020$WDay~DataSumWind2020$Day)
plot(Pingo2021$`Wind vel (m/s)`~Pingo2021$`DOY dec`, ylim=c(0,14), type
   = "l", lty = 1, col="lightgrey", xlim=c(175, 283), cex.lab=0.8, cex.
   axis=0.8,
     xlab="DOY", ylab=parse(text = "wind ~~speed~~ group('[', m * ~~ s
        ^-1, ']')"))
points(DataSumWind2021$WDay~DataSumWind2021$Day)


#Analyzing the lake temperature
SumWa2020= tapply(Pingo2020$`T water`, Pingo2020$Day, mean)
DataSumWa2020 = data.frame('Day'= row.names(SumWa2020), 'WDay'=
   SumWa2020)
SumWa2021= tapply(Pingo2021$`T water`, Pingo2021$DOY, mean)
DataSumWa2021 = data.frame('Day'= row.names(SumWa2021), 'WDay'=
   SumWa2021)
dev.off()
par(mfrow=c(2,1), mar = c(2.6, 2.6, 1, 1), mgp=c(1.5, 0.5, 0), las=0)
plot(Pingo2020$`T water`~Pingo2020$`Day dec`, ylim=c(0,20), col="
   lightgrey",xlim=c(175, 283),cex.axis=0.8, cex.lab=0.8, type = "l",
   lty = 1, xlab="DOY", ylab="temperature [\circ C]")
points(DataSumWa2020$WDay~DataSumWa2020$Day)
plot(Pingo2021$`T water`~Pingo2021$`DOY dec`, ylim=c(0,20),type = "l",
   lty = 1, col="lightgrey", xlim=c(175, 283),cex.axis=0.8, cex.lab=0.8,
    xlab="DOY", ylab="temperature [\circ C]")
points(DataSumWa2021$WDay~DataSumWa2021$Day)


#Analyzing the EC
par(mfrow=c(2,1), mar = c(2.6, 2.6, 1, 1), mgp=c(1.5, 0.5, 0), las=0)
SumEc2020= tapply(Pingo2020$`EC mS/cm`, Pingo2020$Day, mean)
DataSumEc2020 = data.frame('Day2'= row.names(SumEc2020), 'EcDay'=
   SumEc2020)
plot(DataSumEc2020$EcDay~DataSumEc2020$Day2, cex.axis=0.8, ylim=c
   (3.5,7.5), xlim=c(175, 283), cex.main=0.7,cex.lab=0.8, xlab="DOY",
   ylab=parse(text = "conductivity ~~ group('[', ms * ~~ cm^-1, ']')"))
SumEc2021= tapply(Pingo2021$`EC mS/cm`, Pingo2021$DOY, mean)
DataSumEc2021 = data.frame('Day2'= row.names(SumEc2021), 'EcDay'=
   SumEc2021)
plot(DataSumEc2021$EcDay~DataSumEc2021$Day2, xlim=c(175, 283), ylim=c
   (3.5,7.5),xlab="DOY", cex.axis=0.8, cex.lab=0.8, ylab=parse(text = "
   conductivity ~~ group('[', ms * ~~ cm^-1, ']')"))


#Analyzing the water level
dev.off()
par(mar = c(2.6, 2.6, 1, 1), mgp=c(1.5, 0.5, 0), las=0)
SumW2020= tapply(Model_2020_Helene$`Level cm`, Model_2020_Helene$Day,
```

```
   mean)
DataSumW2020 = data.frame('Day2'= row.names(SumW2020), 'WDay'= SumW2020)
plot(Model_2020_Helene$`Level cm`~Model_2020_Helene$`Day dec`, cex.axis
   =0.8, type = "l", lty = 1, col="lightgrey", cex.main=0.7,cex.lab=0.8,
    xlab="DOY", ylab="water level [cm]")
points(DataSumW2020$WDay~DataSumW2020$Day2)


#Analyzing the flux which was based on the data of the analyzer
dev.off()
par(mfrow=c(1,2),mar = c(2.6, 2.6, 1, 1), mgp=c(1.5, 0.5, 0))
Methane2020a= tapply(Pingo2020$FCH4_a, Pingo2020$Day, sum)
DataMethane2020a = data.frame('Day'= row.names(Methane2020a), 'FCH4mgDay
   '= Methane2020a)
plot(DataMethane2020a$FCH4mgDay/1475.381~DataMethane2020a$Day, ylim=c
   (0,1500),xlim=c(175, 283), xlab="DOY",cex.lab=0.8, cex.axis=0.8, ylab
   =parse(text = "CH[4]~~flux ~~ group('[', mg * ~~ d^-1* ~~ m^-2, ']')"
   ), col="red")
Methane2021a= tapply(Model_2021n$FCH4_a, Model_2021n$DOY, sum)
DataMethane2021a = data.frame('Day'= row.names(Methane2021a), 'FCH4mgDay
   '= Methane2021a)
plot(DataMethane2021a$FCH4mgDay/1475.381~DataMethane2021a$Day,ylim=c
   (0,1500), xlim=c(175, 283), xlab="DOY", cex.lab=0.8, cex.axis=0.8,
   ylab=parse(text = "CH[4]~~flux ~~ group('[', mg * ~~ d^-1* ~~ m^-2,
   ']')"), col="orange")

#Analyzing the flux which was based on the samples in 2020
dev.off()
par(mar = c(2.6, 2.6, 1, 1), mgp=c(1.3, 0.5, 0))
Methane2020s5= tapply(Pingo2020$FCH4_s5, Pingo2020$Day, sum)
DataMethane2020s5 = data.frame('Day'= row.names(Methane2020s5), '
   FCH4mgDay'= Methane2020s5)
plot(DataMethane2020s5$FCH4mgDay/1475.381~DataMethane2020s5$Day, cex.
   axis=0.6,col="grey", cex.lab=0.7,
     xlab="DOY", ylim=c(0.00001,900), ylab=parse(text = "CH[4]~~flux ~~
        group('[', mg * ~~ d^-1* ~~ m^-2, ']')"))
Methane2020s6= tapply(Pingo2020$FCH4_s6, Pingo2020$Day, sum)
DataMethane2020s6 = data.frame('Day'= row.names(Methane2020s6),'
   FCH4mgDay'= Methane2020s6)
points(DataMethane2020s6$FCH4mgDay/1475.381~DataMethane2020s6$Day, col="
   darkgreen")
legend(x = "bottomright",c("Position Inflow", "Position Outflow"),
       col=c( "grey","darkgreen"), pch = c(1,1), cex=0.6)


#Analyzing the flux which was based on the samples in 2021
dev.off()
par(mar = c(2.6, 2.6, 1, 1), mgp=c(1.3, 0.5, 0))
Methane2021s2= tapply(Pingo2021Newsa$FCH4_s2, Pingo2021Newsa$DOY, sum)
DataMethane2021s2 = data.frame('Day'= row.names(Methane2021s2), '
   FCH4mgDay'= Methane2021s2)
plot(DataMethane2021s2$FCH4mgDay/1475.381~DataMethane2021s2$Day, col="
   green", cex.lab=0.7, cex.axis=0.6,
     xlab="DOY", ylim=c(0,1600),ylab=parse(text = "CH[4]~~flux ~~ group
        ('[', mg * ~~ d^-1* ~~ m^-2, ']')"))
Methane2021s1= tapply(Pingo2021Newsa$FCH4_s1, Pingo2021Newsa$DOY, sum)
DataMethane2021s1 = data.frame('Day'= row.names(Methane2021s1), '
   FCH4mgDay'= Methane2021s1)
```

```
points(DataMethane2021s1$FCH4mgDay/1475.381~DataMethane2021s1$Day, col="
    purple")
Methane2021s3= tapply(Pingo2021Newsa$FCH4_s3, Pingo2021Newsa$DOY, sum)
DataMethane2021s3 = data.frame('Day'= row.names(Methane2021s3), '
    FCH4mgDay'= Methane2021s3)
points(DataMethane2021s3$FCH4mgDay/1475.381~DataMethane2021s3$Day, col="
    blue")
legend(x = "topright",c("Position Inflow", "Position Outflow", "Position
     Margin"),
       col=c( "green","purple", "blue"), pch = c(1,1,1), cex=0.6)

#Analyzing the sensitivity of the diffusion model
dev.off()
par(mfrow=c(3,2), mar = c(4, 4, 2, 1), mgp=c(2.4, 0.8, 0), las=1)
plot(SensitivityNewPSU$FCH4_s1/1475.381*24~SensitivityNewPSU$`S (PSU)`,
    ylim=c(0,500), main="PSU", cex.axis=1, cex.lab=1, cex.main=1, ylab=
    parse(text = "CH[4]~~flux ~~ group('[', mg * ~~ d^-1* ~~ m^-2, ']')")
    , xlab="practical salinity unit [no unit]")
points(SensitivityNewPSU$FCH4_5/1475.381*24~SensitivityNewPSU$S_5, ylim=
    c(0,500), col="blue")
points(SensitivityNewPSU$FCH4_10/1475.381*24~SensitivityNewPSU$FCH4_10,
    ylim=c(0,500), col="red")
plot(SensitivityNewT$FCH4_s1/1475.381*24~SensitivityNewT$`T water`, ylim
    =c(0,500), main="Water Temperature", cex.axis=1, cex.lab=1, cex.main
    =1, ylab=parse(text = "CH[4]~~flux ~~ group('[', mg * ~~ d^-1* ~~ m
    ^-2, ']')"), xlab="temperature [\circ C]")
points(SensitivityNewT$FCH4_5/1475.381*24~SensitivityNewT$T5, ylim=c
    (0,500), col="blue")
points(SensitivityNewT$FCH4_10/1475.381*24~SensitivityNewT$T10, ylim=c
    (0,500), col="red")
plot(SensitivityNewWind$FCH4_s1/1475.381*24~SensitivityNewWind$`Wind vel
     (m/s)`, ylim=c(0,500), main="Wind Speed", cex.axis=1, cex.lab=1, cex
    .main=1, ylab=parse(text = "CH[4]~~ flux ~~ group('[', mg * ~~ d^-1*
    ~~ m^-2, ']')"), xlab=parse(text = "wind ~~speed~~ group('[', m * ~~
    s^-1, ']')"))
points(SensitivityNewWind$FCH4_5/1475.381*24~SensitivityNewWind$Wind_5,
    ylim=c(0,500), col="blue")
points(SensitivityNewWind$FCH4_10/1475.381*24~SensitivityNewWind$Wind_
    10, ylim=c(0,500), col="red")
plot(SensitivityNewPCH4$FCH4_s1/1475.381*24~SensitivityNewPCH4$pCH4,
    ylim=c(0,500), main="Atmospheric Methane Concentration", cex.axis=1,
    cex.lab=1, cex.main=1, ylab=parse(text = "CH[4] ~~flux ~~ group('[',
    mg * ~~ d^-1* ~~ m^-2, ']')"), xlab=parse(text = "CH[4] ~~
    concentration~~ group('[', ppm, ']')"))
points(SensitivityNewPCH4$FCH4_5/1475.381*24~SensitivityNewPCH4$pCH4_5,
    ylim=c(0,500), col="blue")
points(SensitivityNewPCH4$FCH4_10/1475.381*24~SensitivityNewPSU$FCH4_10,
     ylim=c(0,500), col="red")
plot(SensitivityNewCh4$FCH4_s1/1475.381*24~SensitivityNewCh4$CH4_3,
    ylim=c(0,500), main="Concentration of Dissolved Methane ", cex.axis
    =1, cex.lab=1, cex.main=1, ylab=parse(text = "CH[4] ~~flux ~~ group
    ('[', mg * ~~ d^-1* ~~ m^-2, ']')"), xlab=parse(text = "CH[4]~~
    concentration ~~ group('[', mg * ~~ l^-1, ']')"))
points(SensitivityNewCh4$FCH4_5/1475.381*24~SensitivityNewCh4$CH4_
    5...10, ylim=c(0,500), col="blue")
points(SensitivityNewCh4$FCH4_10/1475.381*24~SensitivityNewCh4$CH4_
    5...11, ylim=c(0,500), col="red")
plot(SensitivityNewP$FCH4_s1/1475.381*24~SensitivityNewP$`Pressure (mbar
```

```
    )‘,  ylim=c(0,500),main="Atmospheric Pressure", cex.axis=1, cex.lab
    =1, cex.main=1, ylab=parse(text = "CH[4] ~~flux ~~ group('[', mg * ~~
     d^-1* ~~ m^-2, ']')"), xlab="pressure [mbar]")
points(SensitivityNewP$FCH4_5/1475.381*24~SensitivityNewP$P5, ylim=c
    (0,500), col="blue")
points(SensitivityNewP$FCH4_10/1475.381*24~SensitivityNewP$P10, ylim=c
    (0,500), col="red")
legend(x = "topleft",dlegen=c("Original Data", "5% Increase", "10%
    Increase"),
        col=c( "black","blue", "red"),lty = c(0,0, 0),
        pch = c(19,19,19), cex=1)



#Chamber measurements data from position A
FluxDatIn2 = Diffusion_Chambers_first_increase

flux_Fit2 = function(MeasDat2){
  DataMeta2 = data.frame(NA)
  fit_CH4 <- lm(CH4_d_umol_m2 ~ DiffTime, data = MeasDat2)
  print('LM fit')

   Fit non-linear model
  dCH4 = diff(MeasDat2$CH4_d_umol_m2)
  x = MeasDat2$DiffTime[-1]
  CH4.nls = nls( dCH4 ~  P2*exp(-P3*x), start = list(P2=0.1, P3 = 1e-2))
  print('NLS Fit')


  DataMeta2$CH4_int_umol_m2_0s <- MeasDat2$CH4_d_umol_m2[1]
  DataMeta2$CH4_slope_umol_m2_s     <- fit_CH4$coefficients[2]
  DataMeta2$CH4_slope_umol_m2_s_exp = coef(CH4.nls)[1]
  DataMeta2$CH4_krate_exp = coef(CH4.nls)[2]


  DataMeta2$CH4_lm_SS = sum(I(resid(fit_CH4))^2)
  yfit2 = MeasDat2$CH4_d_umol_m2[1] + cumsum(coef(CH4.nls)[1]*exp(-coef(
     CH4.nls)[2]*x))
  DataMeta2$CH4_nls_SS = sum(I(yfit2 - MeasDat2$CH4_d_umol_m2[-1])^2)
  DataMeta2$CH4_rsquared  <- summary(fit_CH4)$r.squared

  return(DataMeta2)
}

FluxOut2 = flux_Fit2(FluxDatIn2)


x = FluxDatIn2$DiffTime[-1]

yfit2 = FluxDatIn2$CH4_d_umol_m2[1] +
  cumsum(FluxOut2$CH4_slope_umol_m2_s_exp*exp(-FluxOut2$CH4_krate_exp*x)
     )
plot(FluxDatIn2$DiffTime, FluxDatIn2$CH4_d_umol_m2 *(8.314*282.54*3.14*
    0.15*0.15/3000), cex.axis=0.7, cex.lab=0.7, ylab=parse(text = "CH[4]~
    ~Concentration ~~ group('[', ppm , ']')"), xlab='time [sec]')
lines(x, yfit2 *(8.314*282.54*3.14*0.15*0.15/3000), col='red')
lines(x, (FluxOut2$CH4_int_umol_m2_0s + FluxOut2$CH4_slope_umol_m2_s*x)*
    (8.314*282.54*3.14*0.15*0.15/3000), col='blue')
```

```
legend("topleft", c("Linear regression","Exponential regression"), lty =
    c(1,1), cex=0.7, col = c("blue","red"))

coef(yfit2)

#Chamber measurements data from position B
FluxDatIn3 = Diffusion_Chambers_second_increase


flux_Fit3 = function(MeasDat3){
  DataMeta3 = data.frame(NA)
  fit_CH4 <- lm(CH4_d_umol_m2 ~ DiffTime, data = MeasDat3)
  print('LM fit')

  dCH4 = diff(MeasDat3$CH4_d_umol_m2)
  x = MeasDat3$DiffTime[-1]
  CH4.nls = nls( dCH4 ~  P2*exp(-P3*x), start = list(P2=0.1, P3 = 1e-2))
  print('NLS Fit')


  DataMeta3$CH4_int_umol_m2_0s <- MeasDat3$CH4_d_umol_m2[1]
  DataMeta3$CH4_slope_umol_m2_s     <- fit_CH4$coefficients[2]
  DataMeta3$CH4_slope_umol_m2_s_exp = coef(CH4.nls)[1]
  DataMeta3$CH4_krate_exp = coef(CH4.nls)[2]


  DataMeta3$CH4_lm_SS = sum(I(resid(fit_CH4))^2)
  yfit3 = MeasDat3$CH4_d_umol_m2[1] + cumsum(coef(CH4.nls)[1]*exp(-coef(
     CH4.nls)[2]*x))
  DataMeta3$CH4_nls_SS = sum(I(yfit3 - MeasDat3$CH4_d_umol_m2[-1])^2)
  DataMeta3$CH4_rsquared  <- summary(fit_CH4)$r.squared

  return(DataMeta3)
}

FluxOut3 = flux_Fit3(FluxDatIn3)


x = FluxDatIn3$DiffTime[-1]

yfit3 = FluxDatIn3$CH4_d_umol_m2[1] +
  cumsum(FluxOut3$CH4_slope_umol_m2_s_exp*exp(-FluxOut3$CH4_krate_exp*x)
     )
plot(FluxDatIn3$DiffTime, FluxDatIn3$CH4_d_umol_m2 *(8.314*282.54*3.14*
    0.15*0.15/3000), cex.axis=0.7, cex.lab=0.7,ylab=parse(text = "CH[4]~~
    Concentration ~~ group('[', ppm, ']')"), xlab='time [sec]')
lines(x, yfit3 *(8.314*282.54*3.14*0.15*0.15/3000), col='red')
lines(x, (FluxOut3$CH4_int_umol_m2_0s + FluxOut3$CH4_slope_umol_m2_s*x)*
    (8.314*282.54*3.14*0.15*0.15/3000), col='blue')
legend("topleft", c("Linear regression","Exponential regression"), lty =
    c(1,1), cex=0.7, col = c("blue","red"))
```

Selbstständigkeitserklärung

Ich versichere, dass ich, Helene Köhnen, die Bachelorarbeit zum Thema "Seasonal methane emissions from Lagoon Pingo West in Svalbard" im 8. Semester selbstständig und nur mit den angegebenen Quellen und Hilfsmitteln angefertigt habe. Alle Stellen der Arbeit, die ich aus diesen Quellen und Hilfsmitteln dem Wortlaut oder dem Sinne nach entnommen habe, sind kenntlich gemacht und in den Referenzen aufgeführt. Weiterhin versichere ich, dass weder ich noch andere diese Arbeit weder in der vorliegenden noch in einer mehr oder weniger abgewandelten Form als Leistungsnachweise in einer anderen Veranstaltung bereits verwendet haben oder noch verwenden werden. Die "Richtlinie zur Sicherung guter wissenschaftlicher Praxis für Studierende an der Universität Potsdam (Plagiatsrichtlinie) - Vom 20. Oktober 2010", im Internet unter `http://uni-potsdam.de/ambek/ambek2011/1/Seite7.pdf`, ist mir bekannt. Es handelt sich bei dieser Arbeit um meinen ersten Versuch.